Aeolian Research 54 (2022) 100770

Contents lists available at ScienceDirect

Aeolian Research

journal homepage: www.elsevier.com/locate/aeolia

Depositional timing and palaeoclimate interpretation of the Tamala Limestone aeolianites in Shark Bay, Western Australia

Lucas Vimpere *, Nicolò Del Piero, Aymeric Le Cotonnec, Pascal Kindler, Sébastien Castelltort

Department of Earth Sciences, University of Geneva, Rue des Maraîchers 13, 1205 Geneva, Switzerland

ARTICLE INFO

Keywords:
Aeolianite
Pleistocene
Palaeoclimate
Western Australia
Tamala Limestone
Shark Bay

ABSTRACT

The carbonate units grouped under the name "Tamala Limestone" outcrop for a thousand kilometres along the coast of Western Australia. The extensive Zuytdorp Cliffs shaping the northern half of the coastline up to Shark Bay expose and offer an exceptional access to the stratigraphy of this formation.

The regional survey of the Shark Bay region, which combines both stratigraphic and sedimentological analyses, reveals that the Tamala Limestone is a dry accumulating aeolian system composed of large transverse dunes migrating parallel to the prevailing winds. Accordingly, the amino acid-data show an aging of the units towards the east. Episodes of carbonate aeolian sedimentation correlate with the successive glacial intervals of the Pleistocene whilst paleosols are correlated with breaks in the sedimentation during interglacial intervals.

Palaeoclimate reconstructions reveal that sea level and sea surface temperature of the Indo-Pacific Warm Pool were lower during glacial intervals. The weakened Leeuwin Current, which flows along the western coast of Australia and is the main source of precipitation, contributed to the aridification of the region. Consequently, and associated with a northward migration of the Hadley and Ferrel cells, periods of glaciation were drier. By contrast, paleosols developed through dissolution of the carbonate units during more humid interglacial intervals.

1. Introduction

The Tamala Limestone is a Mid- to Upper-Pleistocene calcareous formation predominantly comprising a complex of stacked aeolian units that is exposed along much of the Western coast of Australia. Extending from Shark Bay in the north to Esperance in the south, it is considered as to be the widest deposit of aeolianites of this age in the world (Wakelin-King and Webb, 2020). The "Tamala Limestone" formation, as defined by Playford et al. (1976), is exposed along the Zuytdorp Cliffs (Fig. 1), which are likely the longest on Earth with a length of 210 km (Wakelin-King and Webb, 2020) and offer an exceptional insight of the Tamala Limestone's stratigraphy. The type section was defined there at Womerangee Hill where the unit is exposed up to 250 m above the present sea level (Playford et al., 2013). As such, the large exposure of the Tamala Limestone stratigraphy represents a great opportunity to understand the dynamic of coastal aeolianites with respect to local/regional climate in a carbonate ramp context, a model still poorly studied and defined.

Since coastal aeolianites form under specific climate conditions and tend to be well preserved due to carbonate early cementation, they have long been studied as eustatic changes markers around the globe (Brooke, 2001 and references herein). A great majority of them deposited during interglacial periods (Brooke, 2001) although aeolianites in Spain (Fornós et al., 2012; Fumanal, 1995), Israel (Belknapt and Mart, 2021; Engelmann et al., 2001; Frechen et al., 2001; Porat and Wintle, 1995), India (Acharya and Bhatt, 2019), and Australia (Price et al., 2001; Zhou et al., 1994), have been reported of glacial age. Regarding the Tamala Limestone in Shark Bay, no detailed sedimentological study has been carried out to define the type of dunes composing this formation, their development, and their direction of migration despite the past investigations carried out in the region. Few studies have attempted to correlate the aeolian stratigraphy of the Zuytdrop Cliffs with climate and sea-level fluctuations. Based on U-Th dating and amino acid racemization relative dating (AAR), one school of thought correlates the formation of the Tamala Limestone aeolianites to interglacial periods of the Pleistocene and even up to the Late Pliocene for the oldest dunes (Hearty and O'Leary, 2008; Jorgensen, 2012; Lipar and Webb, 2014). The opposing viewpoint correlates the entire formation with the Marine Isotope Stage 8 (MIS 8; 300 to 243 ka BP; Fig. 2) based on Optically Stimulated Luminescence (OSL) ages retrieved from the Zuytdrop Cliffs

* Corresponding author.
E-mail address: Lucas.Vimpere@unige.ch (L. Vimpere).

https://doi.org/10.1016/j.aeolia.2021.100770
Received 6 August 2021; Received in revised form 18 October 2021; Accepted 22 December 2021
Available online 31 December 2021

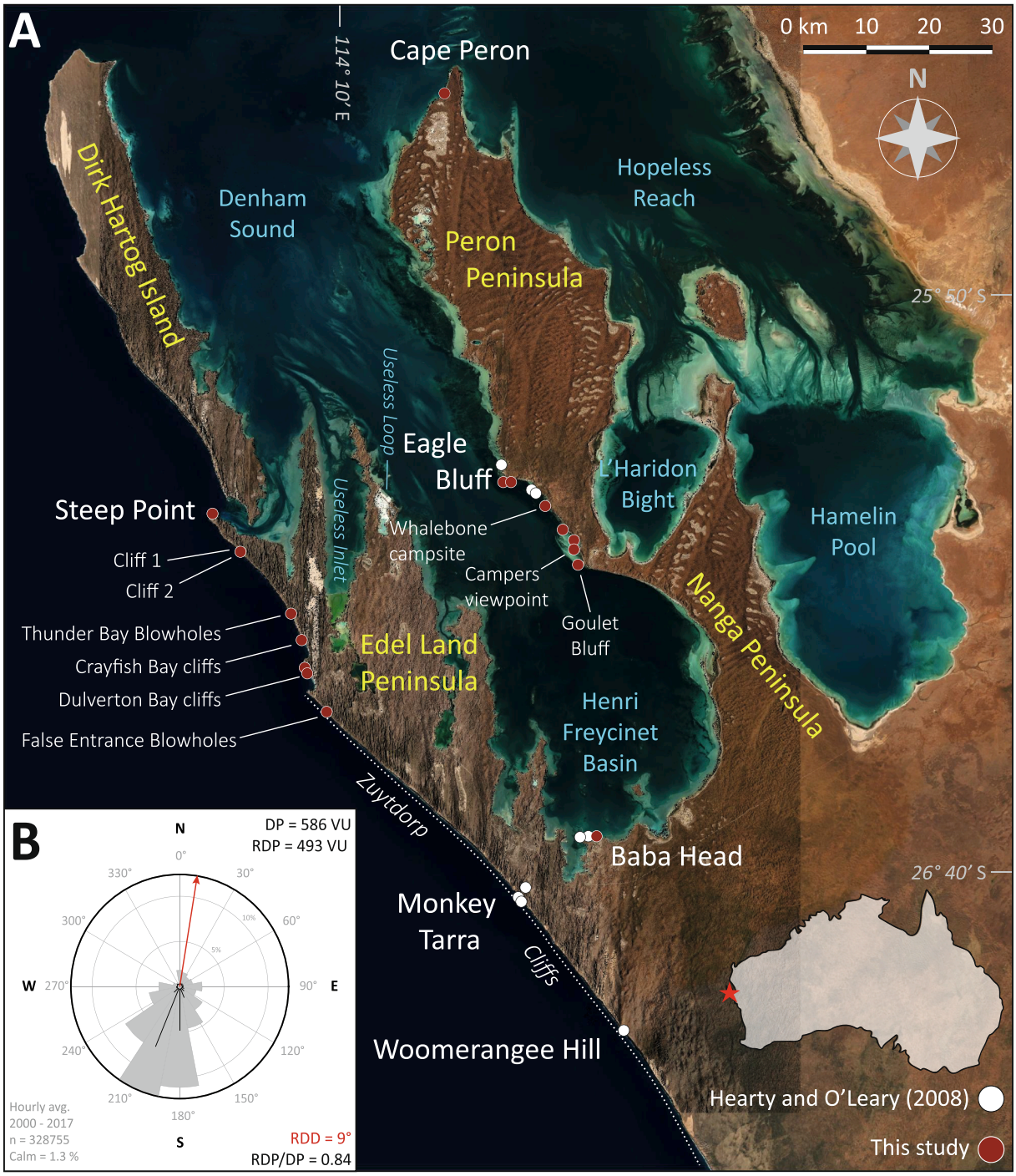

Fig. 1. **A:** Shark Bay texture map generated by the draping of image satellites (Sentinel-2) over the Tandem-X digital elevation model (±12 m; Wessel et al., 2018). The white and red dots represent the studied sites for AAR from Hearty and al. (2008) and this study, respectively. **B:** Wind frequency rose generated from the Carnarvon Airport station data and wind analysis (sand rose) according to the modified Fryberger analysis (Fryberger and Dean, 1979) developed by Kilibarda and Kilibarda (2016). The wind regime is of high-energy (i.e., DP > 400 VU), unidirectional (i.e., RDP/DP > 0.8), and with a preferential direction of sand transport towards the north (RDD = 9°). DP = Drift Potential; RDP = Resultant Drift Potential; RDD = Resultant Drift Direction., all expressed in Vector Units (VU). (For interpretation of the references to colour in this figure legend, the reader is referred to the web version of this article.)

(Playford et al., 2013). However, and according to the authors, the exact timing of deposition has been hindered by problematic ages and the lack of precise dating techniques available for this interval of the Quaternary. Indeed, the Pleistocene stands beyond the range of radiocarbon dating whilst the pristine material suited for U-Th and OSL dating is not always retrievable because of some alteration. Consequently, the connections between aeolian stratigraphy in Shark Bay with glacioeustatic sea levels and palaeoclimate have not been clearly established.

New sections of the Tamala Limestone in the Shark Bay area are presented in this paper with a particular focus on the Zuytdrop Cliffs. This study aims to: (i) investigate the mechanism of transport of dune sands (e.g., migration vs. aggradation), (ii) define the palaeowind direction under which they accumulated, (iii) constrain their timing of deposition and the associated palaeoclimate conditions taking place during their emplacement.

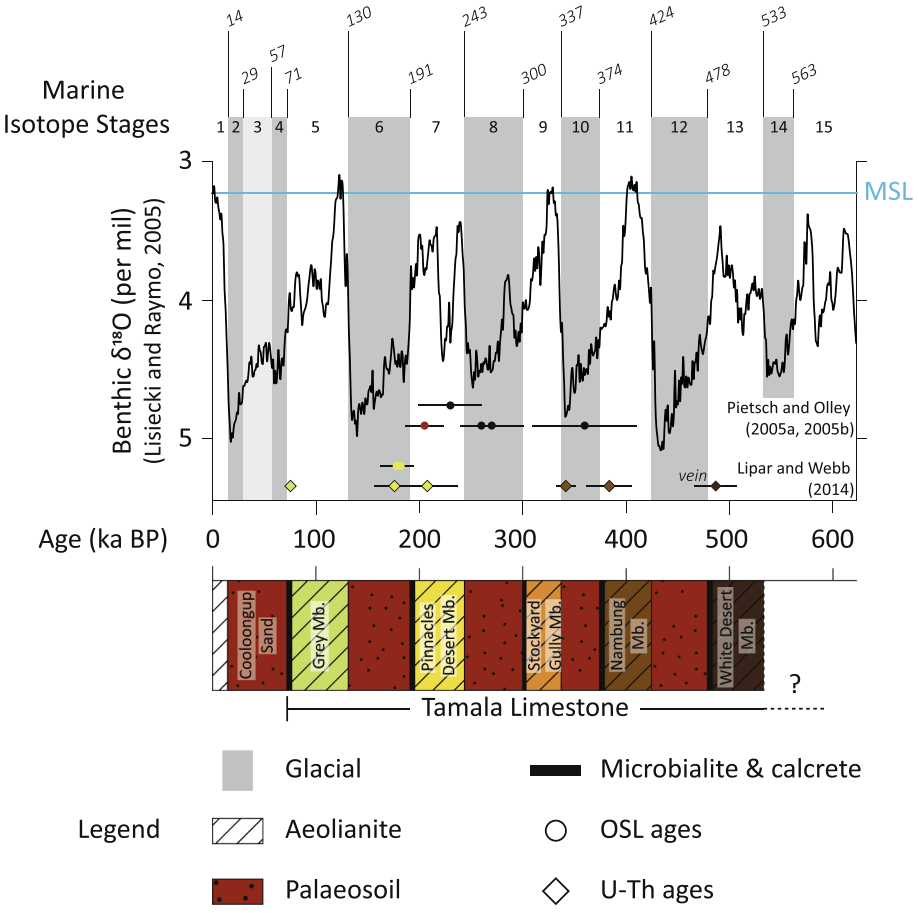

Fig. 2. Glacial-interglacial cycles (Lisiecki and Raymo, 2005) with respect to modern sea level (MSL), and the associated stratigraphic column of the Tamala Limestone defined in the Swan Coastal Plain (Lipar and Webb, 2014). Black and red dots are OSL ages measured in aeolianites and paleosols, respectively, at the Womerangee Hill type section of the Tamala Limestone (Playford et al., 2013). The colours of the OSL and U-Th ages measured by Lipar and Webb (2014) refer to the corresponding members of the Tamala Limestone from which the samples were taken. (For interpretation of the references to colour in this figure legend, the reader is referred to the web version of this article.)

2. Settings

2.1. Geomorphology

Shark Bay is a subtropical region of Western Australia (26 °S) located in the Southern Carnarvon Basin, from which the uniform Carnarvon carbonate ramp extends seaward. Shark Bay shallow sea (average water depth of 9 m) is separated from the Indian Ocean to the west by the Edel Land Peninsula, the Dirk Hartog Island, and the three Dorre, Bernier and Koks islands (Fig. 1-A). The Nanga and the Peron Peninsulas form a complex that divides the sea into two major zones of shallow, metahaline-to-hypersaline waters: Hamelin Pool and Henri Freycinet Harbour Basin. The west coast of Edel Land consists of an escarpment that extends for 210 km from Steep Point in the north to Kalbarri in the south (27.7 °S; 114.2 °E). The Zuytdorp Cliffs reach 250 m in height and sharply truncate the Tamala Limestone, thus offering an exceptional insight into the aeolian stratigraphy. The formation of the Zuytdorp Cliffs has been suggested to be a result of a displacement along the normal Zuytdorp Fault, which was likely active during the Pleistocene and possibly during the early Holocene (Playford, 2003; Playford et al., 2013).

2.2. Quaternary sedimentation

The Quaternary geology of the region predominantly consists of the Pleistocene aeolianites of the Peron Sandstone and the Tamala Limestone, both of which overlie the underlying Tertiary and Cretaceous formations. The Tamala Limestone is mostly found on the Edel Land Peninsula and Dirk Hartog Island, and consist of stacked aeolianites displaying large pristine aeolian structures (e.g., cross-beds) that are separated by paleosol horizons of variable thickness and stiffness, with a texture going from sandy to calcretised (Lipar and Webb, 2014; Smith et al., 2011). During their formation throughout the Quaternary, the Tamala Limestone dunes have been fed by the calcareous, coarse skeletal sands produced on the Carnarvon Ramp off Shark Bay (Hearty and O'Leary, 2008; James et al., 1999; Le Guern, 2004).

The red Peron Sandstone is exposed on the Nanga and Peron Peninsulas where it is irregularly onlapped or interfingered by the Tamala Limestone, notably on the west coast of the Peron Peninsula at Eagle Bluff. It is still debated if the Peron Sandstone is older or is the lateral stratigraphic equivalent of the Tamala Limestone and formed from the concentration of the siliciclastic material through the leaching of carbonate aeolianites.

The bays separated inlets such as Useless Inlet, Useless Loop, or Boat Haven Loop, have been flooded during past marine transgressions like the ones from the Middle and Late Pleistocene (Le Guern, 2004). The high sea levels associated with these intervals led to the deposition of the marine carbonates of the Dampier and the Bibra Formations, respectively, which are sporadically outcropping along the shoreline re-entrants.

Finally, the surface of the region is mostly covered by the Late Pleistocene – Early Holocene Carrarang Sand and Denham Sand (Le Guern, 2004; Playford et al., 2013). The Carrarang Sand is a carbonate sand that composes the seif, parabolic, barchan, massive and undulating dunes on Edel Land Peninsula whilst the Denham Sand is the red sand forming the large parabolic and transverse dunes on the Peron Peninsula (Playford et al., 2013). Most of the Carrarang and Denham Sand dunes, which presently form the surface topography of Shark Bay, are stabilised by vegetation.

2.3. Climate

The climate in Western Australia is mostly arid but is also under the influence of the westerlies that bring rainfall during different seasons

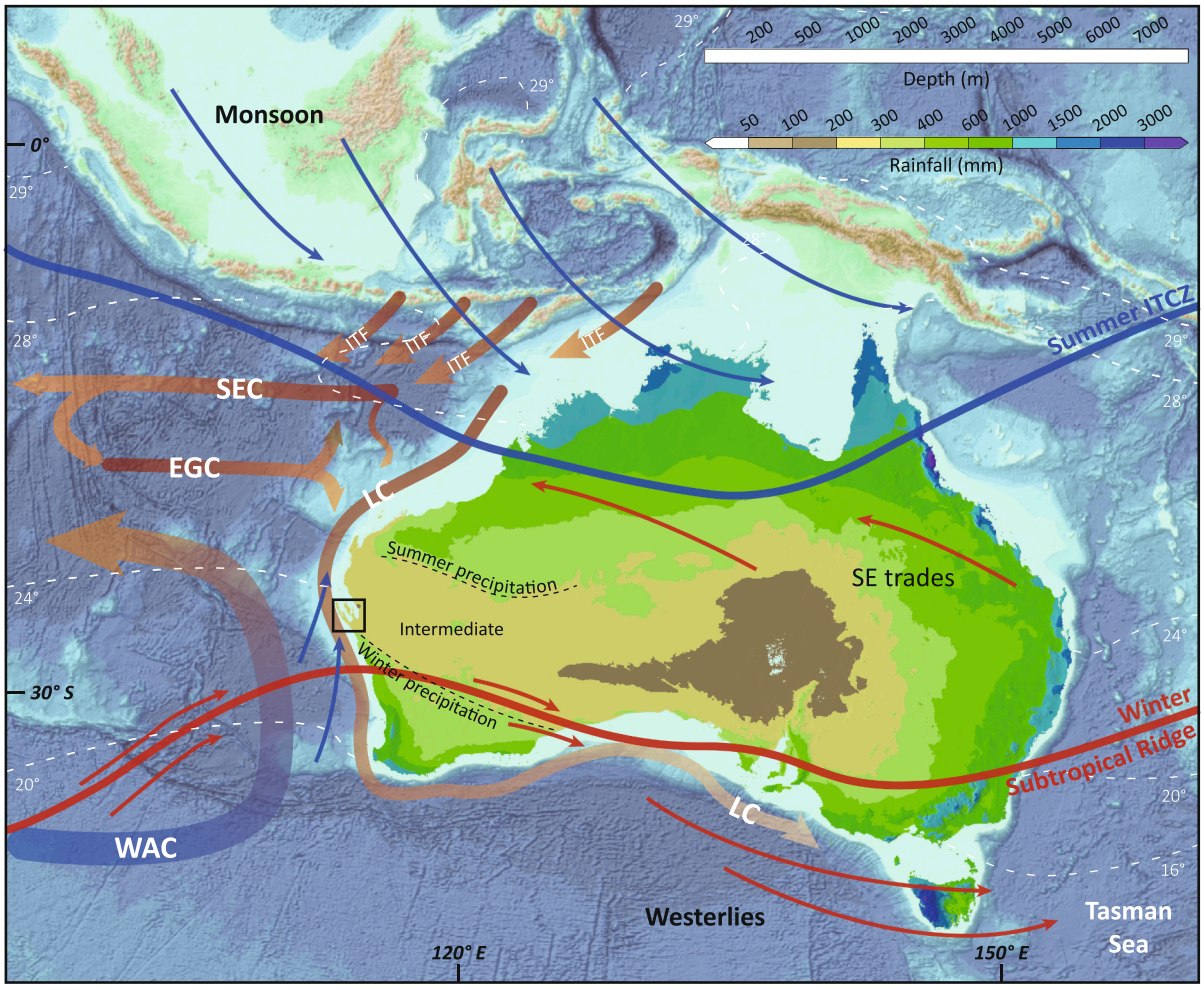

Fig. 3. Map of Australia and Southeast Asia showing the bathymetry (GEBCO Grid), the multi-decadal rainfall map of Australia, and the prevailing atmospheric and oceanic circulation features. The rainfall map is based on 30-year averages calculated over the 1986–2015 period (Australian Bureau of Meteorology: www.bom.gov.au). The limits between the different rainfall zones of Western Australia are represented by the black dashed lines (van der Kaars and De Deckker, 2002). White dashed lines indicate the modern mean annual SST estimates (World Ocean Atlas, 1998; Barrows and Juggins, 2005) with the 28 °C line delimitating the IPWP. Prevailing summer (blue) and winter (red) winds, including summer ITCZ and winter Subtropical Ridge positions, are indicated (modified from Courtillat et al., 2020). Major oceanographic currents include: ITF = Indonesian Throughflow; SEC = Indian and Pacific Ocean South Equatorial Current; EGC = East Gyral Current; WAC = Western Australian Current; LC = Leeuwin Current (modified from Petrick et al., 2019). (For interpretation of the references to colour in this figure legend, the reader is referred to the web version of this article.)

depending on the latitude (Fig. 3). During the austral summer, the southward migration of the Intertropical Convergence Zone (ITCZ) brings monsoon rain and westerlies in the north whilst Southwest Australia remains dry and hot (Fig. 3; Courtillat et al., 2020; Reeves et al., 2013). During the austral winter, precipitation are concentrated in the south (McBride, 1987; Suppiah, 1992) when both the ITCZ and the limit of the subtropical ridge move northward. The strong westerlies and the cold, humid fronts associated with a zone of high pressure are then displaced towards the centre of the country (Fig. 3).

Other large climate systems with a planetary scale influence control the aridity in Western Australia. Indeed, the strength and westward position of westerlies, and thus the amount of moisture brought onto the continent, is also influenced by the Indian Ocean Dipole (IOD). During a positive phase, which occurs every 7.5 years in average, the sea surface temperatures (SST) are lower in the eastern Indian Ocean region than in the western part, which causes droughts in Australia through the suppression of the local convection and the reduction of precipitation (Cai et al., 2014). The Australian summer monsoon (ASM) relies on the moisture generated by the Indo-Pacific Warm Pool (IPWP), which is an extended zone of warm (≥28 °C; Yan et al., 1992) surface waters characterised by low salinity and nutrient content. The IPWP is often referred as the "heat engine" or as the "steam engine" of the world because of the high convective clouds that are generated above it and constitute the source for the monsoon rainfall (De Deckker, 2016). The Indonesian Throughflow (ITF) transports a part of the IPWP waters along the coast of Western Australia (Current et al., 1996; Gordon and Fine, 1996; Spooner et al., 2005; Wijffels et al., 2002), where it eventually mixes with water from the central Indian Ocean to form the Leeuwin Current (LC). The latter is a surface current of slightly salted, warm waters that flows southward following the coastline and preventing upwelling (Godfrey and Ridgway, 1985; Tomczak and Godfrey, 2003). It is weakest during the austral summer, when the opposite southeasterlies are the strongest and the ITCZ is in its southern position. Since the contraction/expansion of the IPWP and the intensity of the ITF are strongly linked to the IOD phases and the El Niño-Southern Oscillation, so is the Leeuwin Current (Saji et al., 1999; Webster et al., 1999) being strengthened during la Niña and weakened during el Niño events (Spooner et al., 2011). Particularly strong events dominated by La Niña makes the LC strong enough to extend up to the southern coast of Australia and the Tasman Sea (De Deckker et al., 2012).

Shark Bay is located between the summer and winter precipitation latitude zones (Fig. 3), where the mean annual rainfall is 230 mm, and

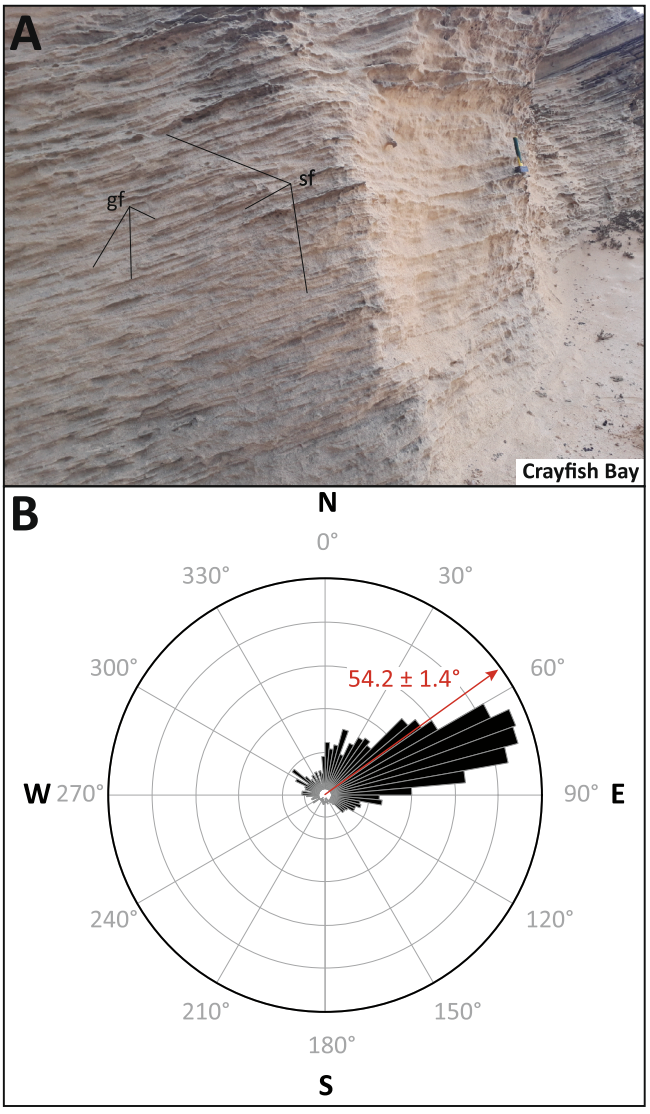

Fig. 4. A: Typical sedimentary structures of the Tamala Limestone exposed along the Zuytdorp Cliffs include the planar-tabular cross-beds, which are constituted by an alternation of sandflow (sf) and finer grainfall (gf) strata. **B:** Rose diagram of the 1832 cross-beds dip directions measured on 3D models generated for four locations of the Zuytdorp Cliffs: Steep Point, Cliff 1, Cliff 2, and False Entrance Blowholes (Fig. 1). The von Mises probability density function indicates that dunes of the Tamala Limestone were migrating ENE.

the mean annual evaporation rate reaches up to 2000–3000 mm (Australian Bureau of Meteorology: www.bom.gov.au). The climate in the region is defined as semi-arid with hot and dry austral summers (from November to March) that contrast with mild austral winters (from April to October) during which most of the precipitation is concentrated. In the region of Shark Bay, the evaporation of the warm LC waters is a key contributor to the winter precipitation, when it is the strongest. During this period, the southerly winds that blow in the opposite direction of flow during the whole year are the weakest (Fig. 1-B; Appendix A).

3. Methods

3.1. 3D models

High-resolution virtual outcrop models were generated using Unmanned Aerial Vehicle (UAV) imagery. The UAV used is a DJI™ Mavic Pro Platinum drone equipped with an onboard camera with a 12.71 M pixels, 1/2.3″ (CMOS) sensor and a 78.8° FOV, 26 mm f/2.2 lens with

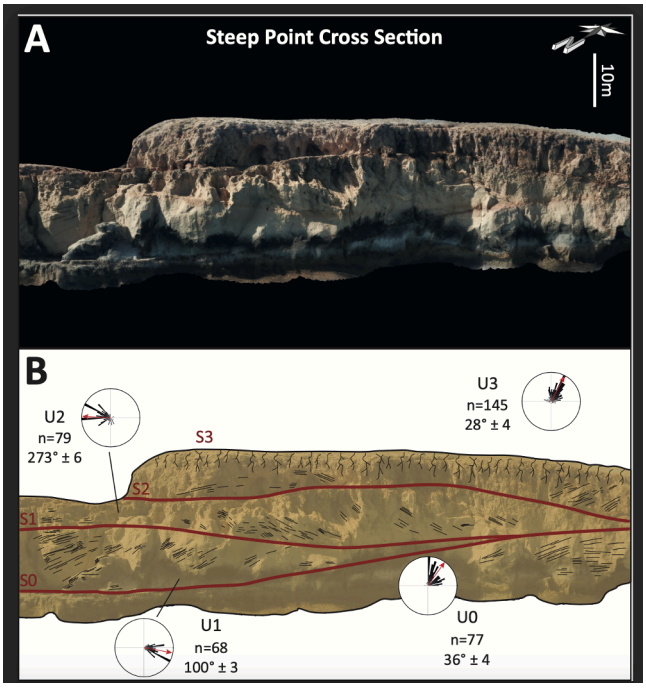

Fig. 5. The 3D model (**A**) of Steep Point and the (**B**) stratigraphic interpretation showing the distribution of the measured cross-strata dip directions for each unit, along with the mean direction vectors (red arrows). (For interpretation of the references to colour in this figure legend, the reader is referred to the web version of this article.)

limited distortion. Still pictures are acquired in a portion of a circle facing the outcrop faces, at 10 to 30 m away from the rock face. In total, 361 photographs were taken of the False Entrance Blowholes, 65 of the Cliff 1, 112 for the Cliff 2, and 414 of the Steep Point outcrops. Those photographs are then processed using Agisoft Metashape™, in which they are aligned, georeferenced and orientated. Then, a dense point cloud is generated for each outcrop, at this stage algorithmic artefacts, commonly water and/or sky-related, as well as isolated points are cleaned. Finally, a mesh is created using the clean point cloud, and a draping texture is generated. The final model is georeferenced then exported to be processed in VRGS™ (Virtual Reality Geoscience Studio) to measure the dip and dip direction of cross-beds. Mean direction vectors for each unit were calculated by applying a von Mises probability density function to the data.

3.2. Whole-rock amino acid racemization (AAR) dating

Altogether, 48 samples were retrieved from aeolianites of the Tamala Limestone, using a hammer and a chisel. A total of 34 samples were collected within aeolian units along vertical transects when rappelling down the Zuytdorp Cliffs. Due to technical limitations, the samples (~1 kg) are randomly distributed along the transects. Considering their exposure to the elements (wind, spray, varying temperature, and humidity), the sampling was done away from paleosol levels (>1 m below) and a 20 cm-deep square was first carved in the cliffs at each sample location to limit a potential bias. Samples were consistently retrieved within sandflow/grainflow alternation. The whole-rock (WR) approach seems preferable considering the skeletal nature of the dominant material. Organisms have control over the symmetry of amino acids contained in their shells (D = right-handed; L = left-handed), which influences the initial DL ratios (Hearty and Kaufman, 2009). The WR-AAR method averages the DL ratios of all the organisms, matrix and cement constituting the samples, resulting in an estimation of the average age of deposition of the sediment. Since cement can yield to

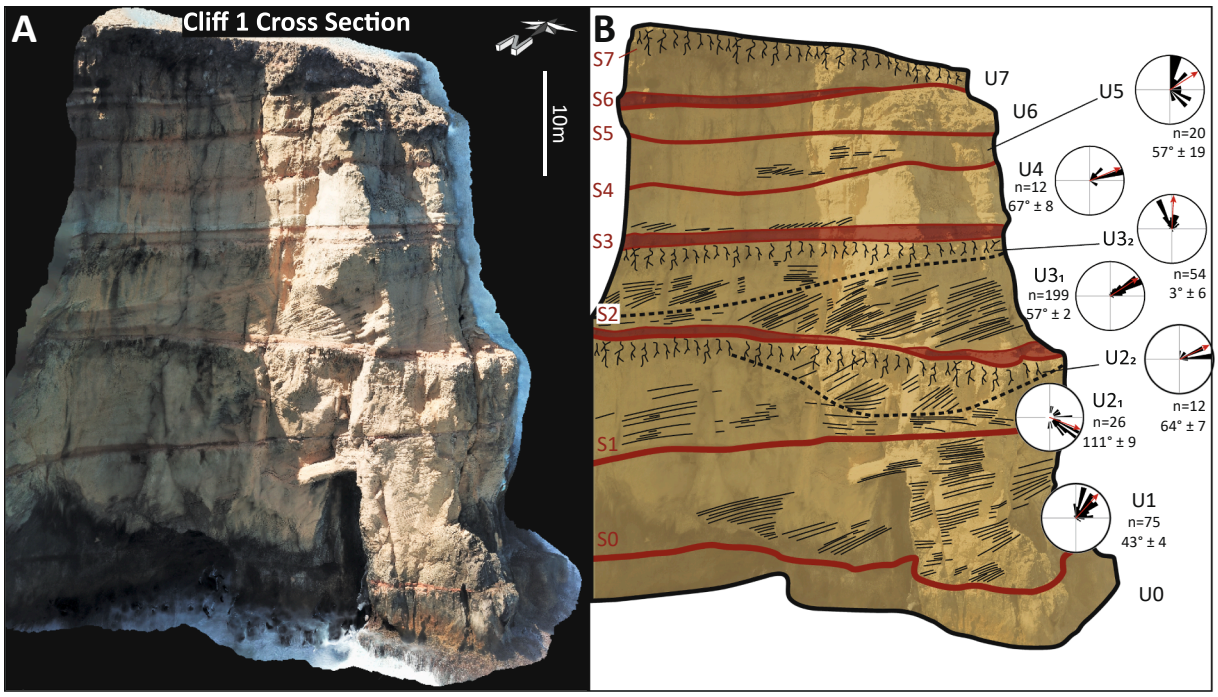

Fig. 6. Photogrammetry-generated 3D model (A) of Cliff 1 next to the stratigraphic interpretation and dip direction measurements (B).

significantly lower A/I ratios, only the 250–850 μm fraction of the sieved samples was kept so that to exclude fine intergranular cements (Hearty and Kaufman, 2000). Potential contamination by remaining cement was reduced through a bleaching of 30% of their total mass with 2 M HCL. The following step consists of the analyses of two sub-samples for each sample through a 22 h-long hydrolysis. The samples were then sent to the Amino Acid Geochronology Laboratory of the Northern Arizona University where the amino acid content was measured by reverse phase high-performance liquid chromatography (Kaufman and Manley, 1998). The conversion method of Whitacre et al. (2017) was applied to the present data to calculate the Alloisoleucine/Isoleucine (A/I) values in order to compare them with the database provided by Hearty and O'Leary (2008).

4. Results

4.1. Stratigraphy and sedimentology of the Zuytdorp Cliffs sections

The height and the number of units composing the cliffs become greater southward where they reach their maximum at Womerangee Hill, the Tamala Limestone type locality. Generally, the stratigraphy is defined by a stack of carbonate aeolian units that are overlain by subsequent red paleosol horizons. Paleosols range from a light-yellow to deep red colour and can be sandy, nodular or calcretic. They may be rich in rhizoliths or gastropods and reach up to 2 m in thickness. Some less-developed soil horizons are present within the carbonate units where they appear as loose, sandy layers usually light-yellow or light orange in colour. The carbonate units are characterised by high-angle, tabular- to wedge-planar cross-bed sets that are metric to decametric in size. They mostly consist of an alternation of fine-grained grainfall and thicker coarse-grained sandflow strata (Fig. 4-A). A total of 1832 dip and dip directions were measured on four photogrammetric 3D models (Fig. 4-B). These measurements indicate that the majority (55 %) of the cross-beds dip at angles higher than 20°, and 40% at>30°. Most of these beds (80 %) are dipping ENE whereas the second cluster (14.6 %) of orientation indicates a NW direction. The resultant mean vector has an orientation of 54.2 ± 1.4°, which corresponds to a general NE orientation of the cross-strata.

Four discrete units were defined at Steep Point, the northernmost location, where carbonate intervals are about 10 m-thick and underlie thin (~1 m), well-cemented soil horizons (Fig. 5). The mean dip orientation of the cross-beds from the units 0 and 3 is NE whereas units 1 and 2 show an ESE and W orientations, respectively.

South of Steep Point, seven couplets of carbonate-paleosol were identified at Cliff 1 with a thickness ranging from 5 to 15 m (Fig. 6). A bounding surface and a protosoil divide the units 2 and 3, respectively, into four subunits from which orientation measurements were made separately. Overall, the general sedimentary structure of the cliff is pointing ENE, which is also the case for the units 2_2 and 4. The units 1 and 3_1 indicate a NE orientation of cross-beds whereas the ones forming the unit 3_2 are dipping north. Contrary to the others, unit 5 does not present a unimodal distribution of the measured orientations but rather a bimodal one with cross-beds dipping towards the N-NE and SE. Only the unit $U2_1$ indicates a sedimentary structure dipping towards the SE.

Cliff 2 only lies 300 m to the SE from Cliff 1 but displays a more complex stratigraphy. Ten units compose Cliff 2, of which four are subdivided into two or more subunits by bounding surfaces, sometimes represented by protosoils (Fig. 7). Most of the cross-beds are dipping E to NE except for the ones from unit 0 that are dipping N, and from units 6_1, and 9 that are inclined towards the NW.

The southernmost studied cliff, located at False Entrance Blowholes, is composed by 15 units separated by 14 visible paleosol horizons (Fig. 8). All carbonate units show a unimodal distribution of cross-beds orientations uniformly indicating an ENE dip direction.

4.2. Whole-rock AAR

The samples collected in the Shark Bay area have A/I ratios ranging from 0.179 to 1.006, and amino acid concentrations varying from 9 to 633 nM/mg (Table 1). Out of the 48 analysed samples, 24 showed low concentrations of amino acids, defined as < 80 nM/mg (Hearty and O'Leary, 2008), and 4 of them could only be analysed once. Nine other samples had amino acid concentrations below the detection limit. In general, uncertainty becomes greater with a higher A/I ratio, which slightly increases with the amino acid concentration (Fig. 9). Both A/I ratios and the corresponding amino acid concentration values

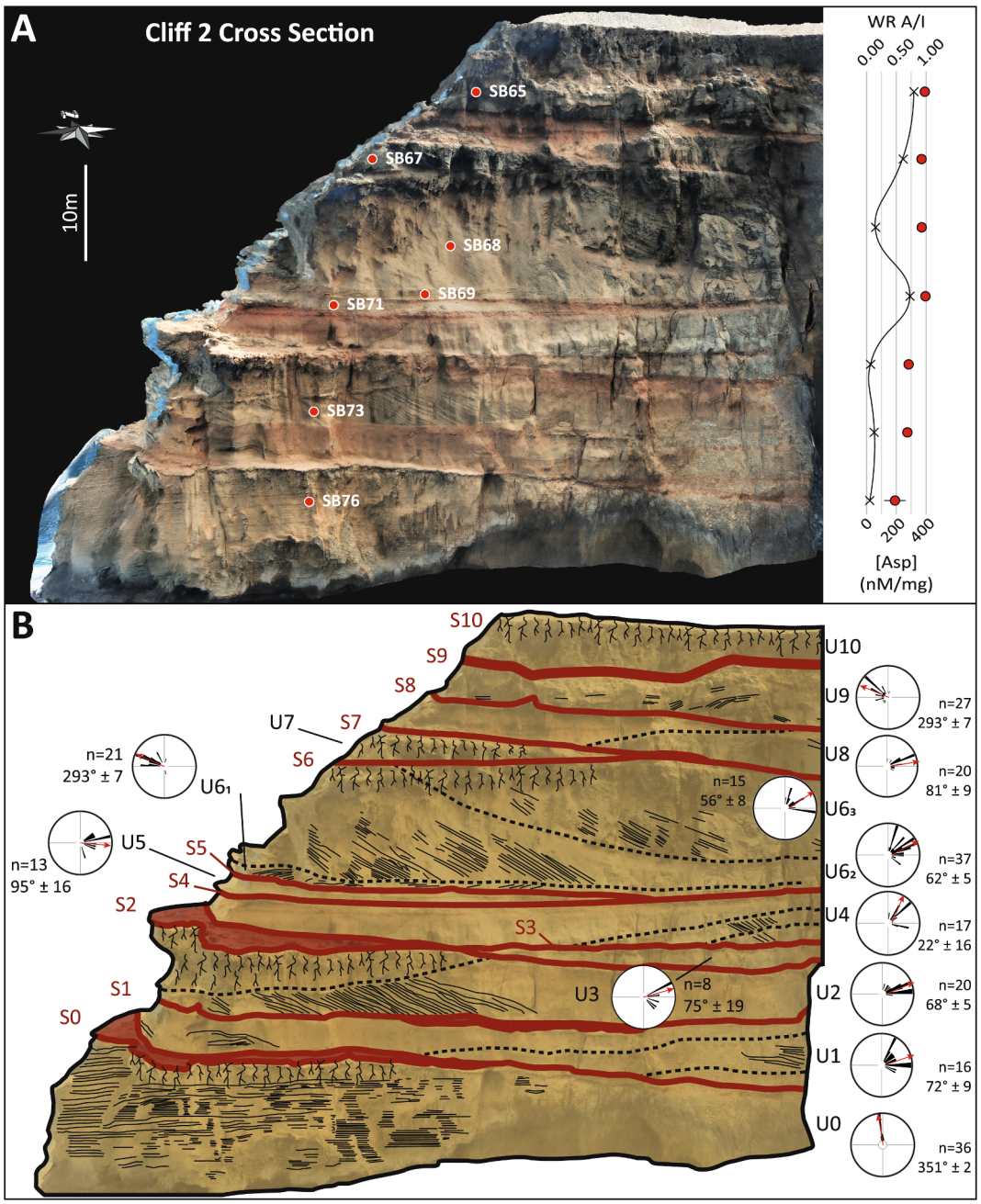

Fig. 7. A: 3D model of Cliff 2 showing the sampled units and the associated A/I values and amino acid concentrations decreasing downwards. **B:** Stratigraphic interpretation of Cliff 2 showing the distribution of the measured cross-strata dip directions for each unit, along with the mean direction vectors (red arrows). (For interpretation of the references to colour in this figure legend, the reader is referred to the web version of this article.)

exponentially decrease towards the east (Fig. 10).

In total, 12 samples were collected from six different sites (Fig. 1) along the cliffs of the west coast of the Peron Peninsula. The Tamala Limestone can be seen overlying the Peron Sandstone at three locations, going from North to South: Eagle Bluff (Fig. 11), an unnamed headland south of the Whalebone Campsite (Fig. 12-A), and another one north of Goulet Bluff that will be referred to as Campers Viewpoint in this study (Fig. 12-B). At Eagle Bluff, the two samples from the same unit of the ESE-facing cliff yielded A/I ratios of 0.464 ± 0.005 and 0.339 ± 0.051, and low concentrations in amino acid (37 and 49 nM/mg). The concentrations in the sample collected within the WNW-facing cliff were below the detection limit therefore no A/I ratio could be retrieved from it. At the Whalebone Campsite, two samples from the limestone that were taken within the fine and the coarse lamina of cross-beds gave ratios of 0.518 ± 0.035 (45 nM/mg) and 0.857 ± 0.132 (24 nM/mg), respectively. South of the Whalebone Campsite, the loose sediment being blown off on top of the red sandstone and the carbonate bluff displayed a ratio of 0.179 ± 0.034 and a low concentration in amino acid (10 nM/mg). Another ratio of 0.538 ± 0.023 (177 nM/mg) was measured from the limestone bluff lying north of the Campers Viewpoint. At the Campers Viewpoint, the limestone and the underlying red calcareous sandstone yielded an A/I value of 0.669 (measured only once, 22 nM/mg) and 0.651 ± 0.027 (20 nM/mg), respectively. Finally, the limestone at Goulet Bluff produced an A/I ratio of 0.408 ± 0.023 and a concentration value of 29 nM/mg.

Along the west coast of the Edel Land Peninsula, six locations were investigated for aminostratigraphy (Fig. 1). The top and the middle units at Steep Point yielded A/I ratios of 1.006 ± 0.019 and 0.881 ± 0.019,

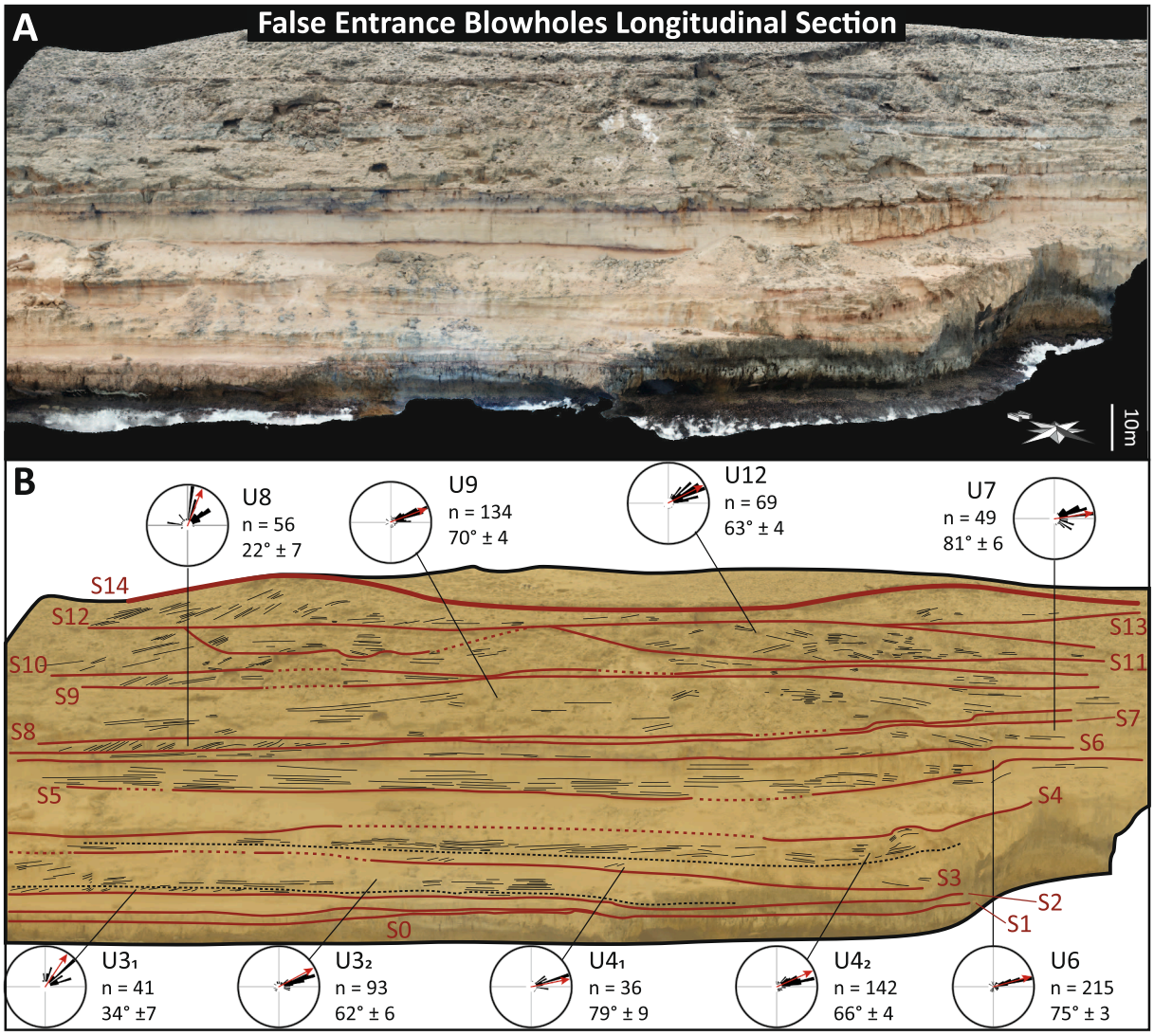

Fig. 8. Model and stratigraphic interpretation of the southernmost studied section at False Entrance Blowholes showing the distribution of the measured cross-strata dip directions for each unit, along with the mean direction vectors (red arrows). (For interpretation of the references to colour in this figure legend, the reader is referred to the web version of this article.)

respectively (Fig. 13-A). The upper unit showed a mean concentration (606 nM/mg) that is nearly twice higher than the one measured in the underlying unit (285 nM/mg). A total of ten samples were collected within the cliffs forming the southernmost studied section at False Entrance Blowholes (Fig. 13-B). The decrease of A/I values from stratigraphically lower units correlates with the decreasing trend in the concentration of amino acids. The carbonate units from Cliff 2 yielded ratios in a descending order of 0.977 ± 0.010, 0.930 ± 0.008, 0.925 ± 0.008, 0.988 ± 0.012, 0.703 ± 0.012, 0.681 ± 0.030, 0.473 ± 0.106 (Fig. 7).

The top and intermediate units of a cliff at Thunder Bay Blowholes gave A/I values of 0.812 ± 0.008 and 0.804 ± 0.016, respectively, with a concentration in amino acids slightly higher in the uppermost unit (Fig. 14-A). The cliffs terminating the beach of Crayfish Bay, also named Epineux Bay, on its northern shore were also investigated (Fig. 14-B). From the top to the base of the Crayfish Bay section, the retrieved A/I values decrease from 0.655 ± 0.016, to 0.497 (measured once), and to 0.461 (measured once), which correlates with the decreasing concentrations in amino acids (30.5, 17, and 9 nM/mg). One sample from an immature protosoil within the uppermost unit, and another one from the unit below had concentrations of amino acids below the detection limit. Finally, the uppermost unit of the cliffs at Dulverton Bay (also named False Entrance) was sampled twice (Fig. 14-C). Samples showed similar concentrations of amino acids (12 and 10 nM/mg) and yielded A/I ratios of 0.545 ± 0.012 and 0.342 (measured once).

Whilst the concentration values in amino acids are evidently decreasing towards the base of the section, the calculated A/I ratios display a greater variability with no clear trend. In descending order, A/I values were calculated at 0.937 ± 0.009, 0.794 ± 0.035, 0.877 ± 0.005, 0.483 ± 0.005, 0.566 ± 0.023, 0.825 ± 0.028, two samples below the detection limit, 0.776 ± 0.011, and 0.822 ± 0.006. Of the corresponding amino acid concentration values, only the first three were above the significative limit of 80 nM/mg.

5. Discussion

5.1. Depositional timing of the Tamala Limestone

So far, two dating methods have been used on samples that were directly retrieved from the Zuytdorp Cliffs. Pietsch and Olley (2005a, 2005b) have reported five Optically Stimulated Luminescence (OSL) ages from the type section of the Tamala Limestone located at Womerangee Hill (Fig. 2; Playford et al., 2013). Measured from the top of the section, the calculated ages are ~ 260 ka at 33 m, 360 ± 30 ka at 85 m,

Table 1
Amino acid concentrations and A/I ratios measured by reverse phase (RP) chromatography on whole-rock samples from Shark Bay, the Geraldton Sandplains, and the Swan Coastal Plain (based on the Interim Biogeographic Regionalisation for Australia, IBRA7). Alloisoleucine/Isoleucine (A/I) values were calculated following a log2 transformation of the DL-Asp ratios, following to the method developed by Whitacre et al. (2017).

Area	Location	Sample ID	Lat.	Long.	DL Asp	±	[Asp]	A/I
Peron	Cape Peron	sb3	−25.5429	113.4910	ND	ND	ND	ND
	Eagle Bluff	sb7	−26.0948	113.5819	ND	ND	ND	ND
		sb8	−26.0948	113.5819	0.586	0.005	37	0.464
		sb11	−26.0948	113.5819	0.520	0.051	49	0.339
		sb13	−26.0949	113.5800	ND	ND	ND	ND
	Whalebone Campsite	sb14	−26.1302	113.6400	0.611	0.035	45	0.518
		sb15	−26.1302	113.6400	0.740	0.132	24	0.857
	S of Whalebone Campsite	sb31	−26.1649	113.6631	0.408	0.034	10	0.179
	N of Campers Viewpoint	sb30	−26.1828	113.6841	0.620	0.023	177	0.538
	Campers ViewPoint	sb20	−26.1977	113.6833	0.673	ND	22	0.669
		sb18	−26.1977	113.6833	0.666	0.027	20	0.651
	Goulet Bluff	sb28	−26.2165	113.6881	0.558	0.023	29	0.408
Edel Land	Baba Head	sb39	−26.6052	113.6925	0.554	0.064	633	0.401
		sb36	−26.6052	113.6925	0.500	0.013	593	0.305
	Steep Point	sb53	−26.1433	113.1591	0.786	0.019	606	1.006
		sb52	−26.1433	113.1591	0.748	0.019	285	0.881
	Cliff 2	sb65	−26.1951	113.1972	0.778	0.010	317	0.977
		sb67	−26.1951	113.1972	0.763	0.008	245	0.930
		sb68	−26.1951	113.1972	0.762	0.008	61	0.925
		sb69	−26.1951	113.1972	0.781	0.012	292	0.988
		sb71	−26.1951	113.1972	0.686	0.012	26	0.703
		sb73	−26.1951	113.1972	0.678	0.030	50	0.681
		sb76	−26.1951	113.1972	0.591	0.106	22	0.473
	Thunder Bay Blowholes	sb51	−26.2875	113.2725	0.725	0.008	202	0.812
		sb50	−26.2875	113.2725	0.722	0.016	186	0.804
	Crayfish Bay	sb47	−26.3252	113.2904	0.668	0.010	30.5	0.655
		sb46	−26.3252	113.2904	ND	ND	ND	ND
		sb41	−26.3245	113.2893	0.602	ND	17	0.497
		sb43	−26.3245	113.2893	0.584	ND	9	0.461
		sb44	−26.3251	113.2897	ND	ND	ND	ND
	Dulverton Bay	sb48	−26.3642	113.2949	0.522	ND	10	0.342
		sb49	−26.3653	113.2961	0.623	0.012	12	0.545
	False Entrance Blowholes	sb62	−26.1925	113.1940	0.765	0.009	235	0.937
		sb64	−26.1925	113.1940	0.719	0.035	219	0.794
		sb63	−26.1925	113.1940	0.746	0.005	243	0.877
		sb54	−26.1925	113.1940	0.595	0.005	20	0.483
		sb55	−26.1925	113.1940	0.632	0.023	65	0.566
		sb56	−26.1925	113.1940	0.729	0.028	32	0.825
		sb58	−26.1925	113.1940	ND	ND	ND	ND
		sb59	−26.1925	113.1940	ND	ND	ND	ND
		sb60	−26.1925	113.1940	0.712	0.011	26	0.776
		sb61	−26.1925	113.1940	0.728	0.006	39	0.822
Southern Beekeeper's Nature Reserve	Aiyennu Cave	sb77	−29.9279	115.0923	0.595	0.000	38	0.482
		sb78	−29.9279	115.0923	ND	ND	ND	ND
Nambung National Park	Pinnacles Desert	sb79	−30.6085	115.1635	ND	ND	ND	ND
		sb80	−30.6096	115.1672	0.499	0.017	152	0.304
		sb82	−30.6090	115.1655	0.208	0.023	14	0.030
		sb83	−30.5992	115.1629	0.367	0.142	167	0.135

270 ± 30 ka at 120 m, 205 ± 18 ka at 132 m, and 230 ± 30 ka at 215 m. Since they show age inversions, these data were assumed problematic by the authors who then concluded that the whole section was likely deposited circa 250 ka ago, which corresponds to the glacial MIS 8.

Subsequently, Hearty and O'Leary (2008) attempted to date samples retrieved from the Monkey Tarra and the Womerangee Hill sections on the Zuytdorp Cliffs by amino acid racemization (AAR). They have interpreted the upper and middle beds of both sections as early Pleistocene in age, based on the measured A/I ratios. The lower beds, however, show low to non-detectable levels of amino acids and may have been deposited during the earliest Pleistocene and/or the Pliocene according to the authors. Problematic A/I values in both the Monkey Tarra and Womerangee Hill sections decrease in stratigraphically lower units, which translates into an age inversion. By analogy with the Bahamas, where the authors have significantly contributed to the development of a stratigraphic model, aeolian units were interpreted as highstand deposits whereas paleosols and calcretes were correlated to glacial periods.

Further south (~600 km) onto the Swan Coastal Plain, five members of the Tamala Limestone have been recognised and dated by both OSL and U-Th over the last 500 ka (Fig. 2; Lipar and Webb, 2014). The Tamala Limestone Formation is subdivided into five members that are stratigraphically separated from each other by paleosols. The whole formation is believed to date from MIS 13 at least to MIS 5, and is capped by the Cooloongup Sand dated to the Last Glacial Period (LGP; MIS 4 to 2), which could correlate with the Denham Sand defined in Shark Bay (Playford et al., 2013). Most of the U-Th ages were retrieved from microbialites capping the aeolian carbonate units and underlying paleosol levels, except for the one obtained in a vein intersecting the White Desert Member. These ages were interpreted by the authors as the end of the periods of aeolian accumulation. Therefore, and in agreement with Hearty and O'Leary (2008), Lipar and Webb (2014) correlated aeolian sedimentation and paleosol formation to interglacial and glacial periods, respectively. By contrast, two OSL ages measured within aeolianites of the Pinnacles Desert Member indicate a deposition during the glacial MIS 6 (Fig. 2).

In the context of this study, only one third of the processed samples showed levels of amino acid concentration that were high enough to ensure trustworthy subsequent A/I ratios (Fig. 9). Most of these are close to the equilibrium value settled at 1.3 (Hearty and Kaufman, 2009, 2000), which makes them less reliable. This is emphasised by an

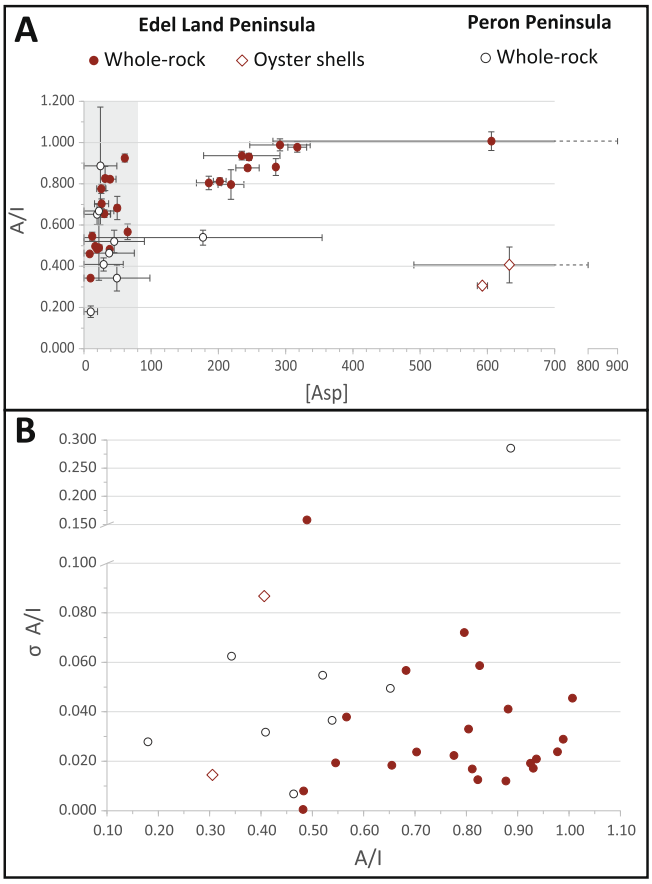

Fig. 9. **A:** A decrease in amino acid concentration correlates with a decrease in the measure DL-Asp ratio and therefore, in the subsequently calculated A/I ratio. The oyster shells were sampled at Baba Head in a shelly storm-surge layer (sb36 and sb39 in Table 1). Samples from the Peron Peninsula show lower amino acid concentrations and A/I ratios compared with the ones from Edel Land Peninsula. **B:** The standard deviation (i.e., uncertainty) expressed as **σ** slightly increases with the A/I value in each location group.

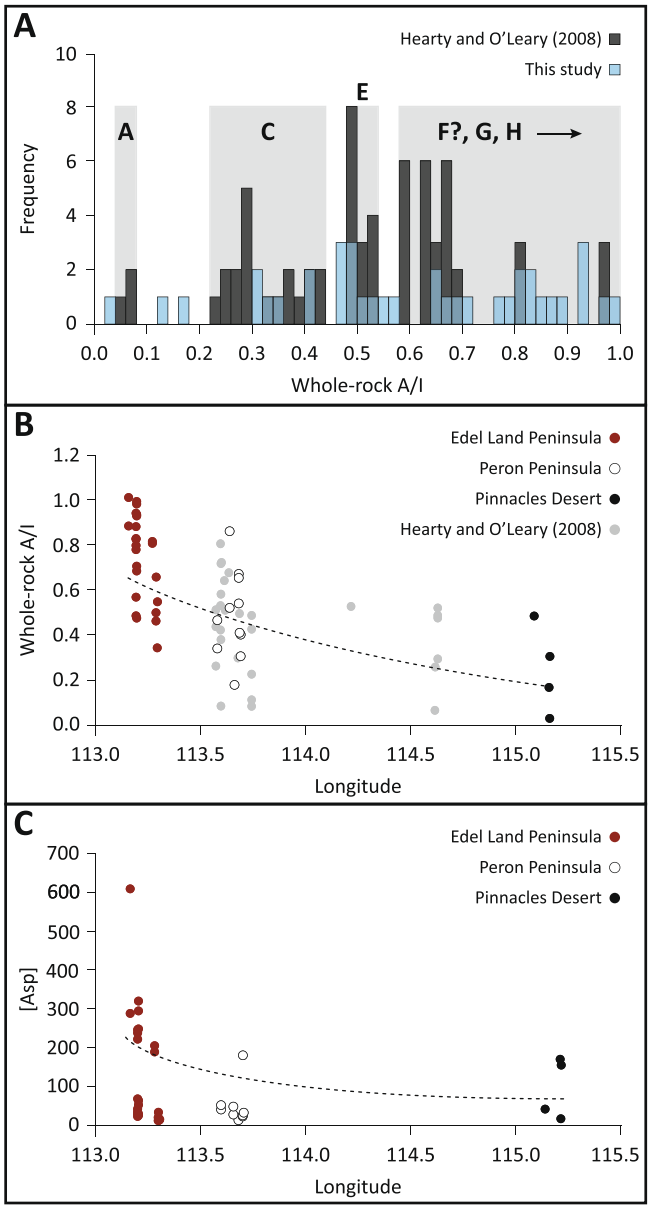

Fig. 10. **A:** Histograms of whole-rock A/I values from this study along with the ratios and aminozones defined by Hearty and O'Leary (2008). The eastward (i.e., inland) decrease in both A/I values (**B**) and amino acid concentrations (**C**) representing the increasing diagenetic state (i.e., aging) of sediments.

uncertainty increasing with A/I values, and ratios being significantly different between samples coming from the same unit (Figs. 11 and 14-C). The distribution of the measured A/I ratios is similar to the one published by Hearty and O'Leary (2008), with values concentrating within the aminozones they have defined for the region (Fig. 10-A). However, our data show inconsistencies such as the bottom unit at Cliff 2 and the top one at Dulverton Bay, both correlating with the aminozone E. The latter was assigned to MIS 5e by Hearty and O'Leary (2008), which would indicate that the entire Tamala Limestone complex in Shark Bay was deposited during this unique highstand. This observation does not corroborate the age interpretations made for the Zuytdorp Cliffs succession by previous authors (Playford, 2013).

Generally, the concentrations in amino acids and the A/I values retrieved from the Tamala Limestone on the Peron Peninsula are lower than the ones measured on samples from the Edel Land Peninsula (Fig. 10-B and C). Lower A/I ratios indicate younger units but the reliability of the measurements is highly dependent of the amino-acid concentration within the carbonate. It is already known that amino acid concentration decreases with the age of the sample and the state of diagenesis (Hearty and Kaufman, 2000; Hearty and O'Leary, 2008; Roof, 1997), so this observation either indicates that carbonate units tend to be older or that the degree of carbonate diagenesis increases towards the East. Previous studies that have been conducted in the Perth Basin have demonstrated that the yellow sand overlying the Tamala Limestone formed by residual accumulation of the siliciclastic material after the dissolution of the carbonate units (Bastian, 2010, 1996, 1994; Newsome, 2000; Playford et al., 2013). The authors pointed out the progressive leach-out of heavy minerals that are most subject to weathering towards the east, so from the youngest to the oldest units. The inland ageing of the units was later confirmed by U-Th dating of successive coastal ridges of the Swan Coastal Plain and the Geraldton Sandplains (Lipar and Webb, 2014). The progressive loss in amino acid observed towards the east in Shark Bay therefore indicates an increase in the diagenetic state of the limestone, which correlates with the inland ageing of the deposits. This is also supported by the systematically observed decrease in both A/I value and amino acid concentration in stratigraphically lower units along the studied transects (Figs. 7 and 13-B). As already suggested by Hearty and O'Leary (2008), the lowering trend of amino acid values is time-dependent and can be used for a relative dating of the Tamala Limestone units. However, further accurate dating will require a robust calibration with absolute dating techniques (e.g., U-Th, or OSL) to compensate for the lack of accuracy of the AAR method. Nevertheless,

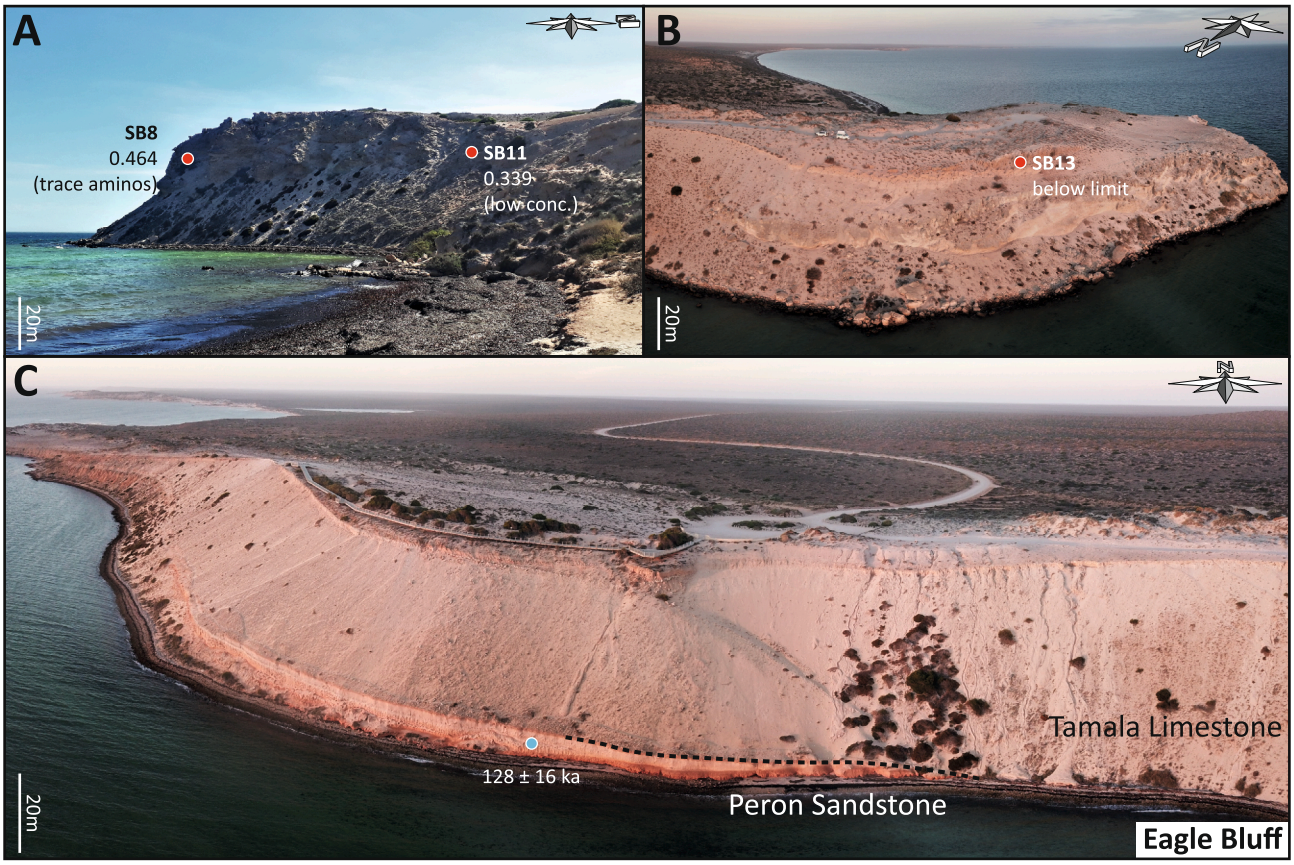

Fig. 11. Three samples from the top carbonate unit at Eagle Bluff were samples within the ESE- and WNW-facing cliffs (**A and B**). **C:** Cliff exposing the Tamala Limestone overlying the Peron Sandstone, from which an OSL age has been retrieved by Pietsch and Olley in 2005 (Playford et al., 2013), at Eagle Bluff.

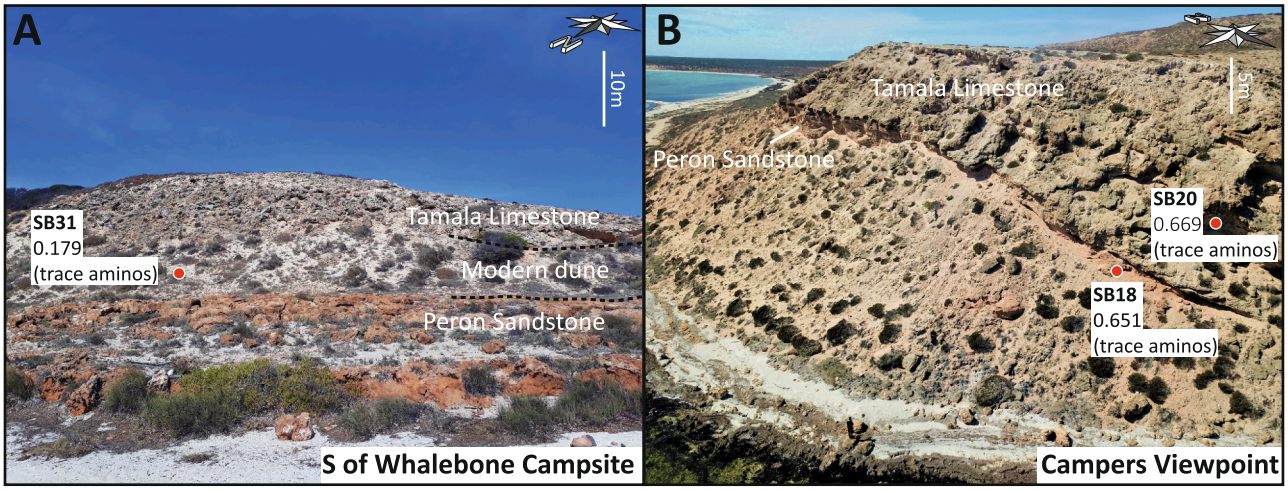

Fig. 12. The Tamala Limestone can be seen overlapping the Peron Sandstone in different locations along the Western Coast of the Peron Peninsula. South of the Whalebone Campsite (**A**), a modern dune feeding from the adjacent beach is presently migrating on top of both the Tamala Limestone and Peron Sandstone. At the Campers Viewpoint, the erosive coast exposes the Peron Sandstone/Tamala Limestone succession along a cliff showing the reworking of sediment on the slope (i.e., boulder and sand). The man standing on a boulder (bottom middle of photo) is 1 m85 tall.

these data refute the interpretation that the carbonate units of the Tamala Limestone at the Zuytdorp Cliffs formed during one single glacial episode (MIS 8, Playford et al., 2013), but rather suggest that deposition took place during various intervals of the Quaternary.

To summarise, age inversions shown by contradictory AAR and OSL dating in Shark Bay result in the age and depositional timing of the Tamala Limestone being poorly constrained. The remoteness and difficulty of access lead to data scarcity, adding to the lack of proper dating technique for such material of Pleistocene age. However, the different dating methods applied to the Zuytdorp Cliffs sediment converge towards a depositional period ranging from the Middle to the Late Pleistocene.

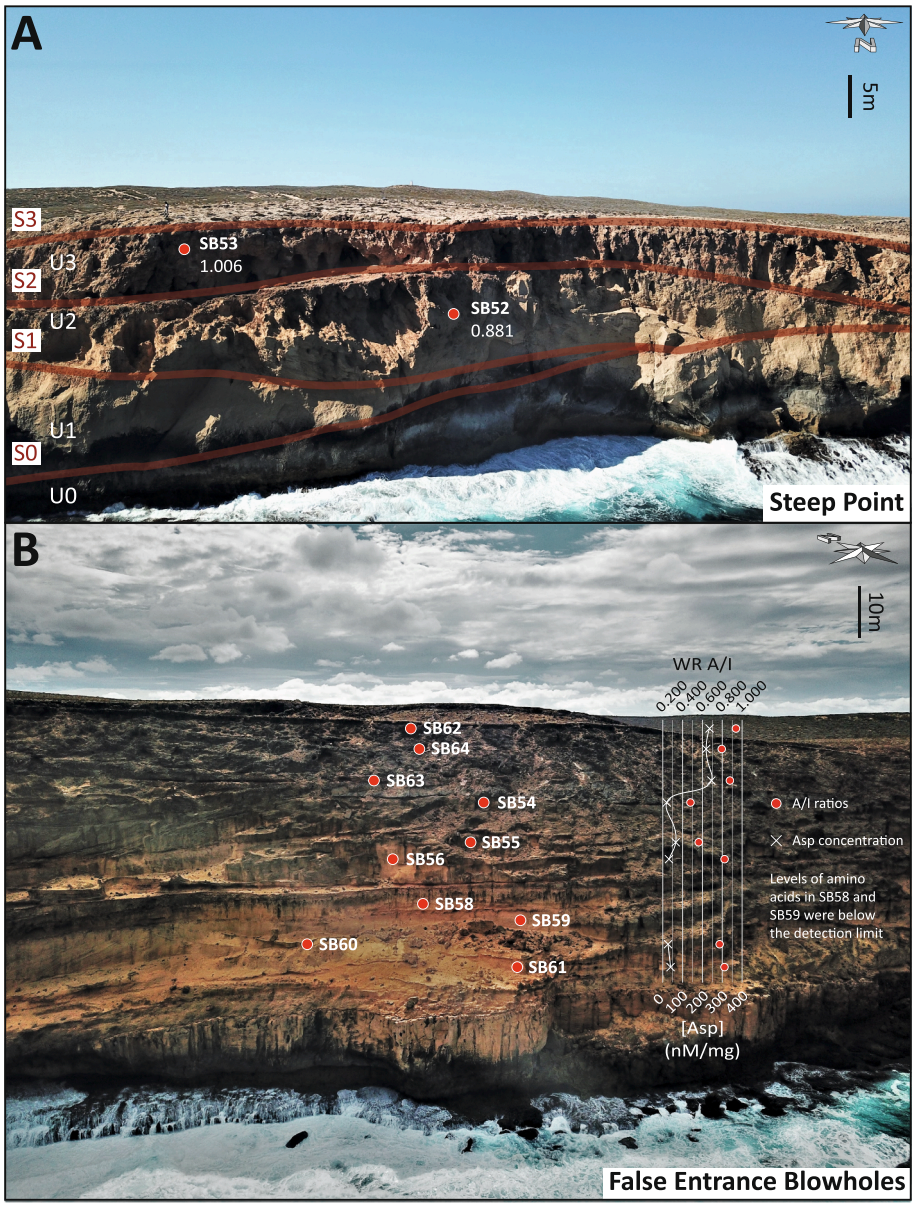

Fig. 13. A: Stratigraphy and A/I values from Steep Point, the northernmost investigated section in this study. Each aeolianite is capped by a red, bioturbated paleosol horizon. **B:** At False Entrance Blowholes, the southernmost studied section, the AAR analysis show the characteristic decrease in amino acid concentrations in the stratigraphically lower units. Whole-rock A/I ratios from the bottom aeolianites are considered unreliable because associated with very low level of amino acids. (For interpretation of the references to colour in this figure legend, the reader is referred to the web version of this article.)

5.2. *Dune type evolution*

The Tamala Limestone exposed along the Zuytdorp Cliffs present the characteristic aeolian alternation of grainfall and sandflow cross-strata (Fig. 4-A; Hunter, 1977; Kocurek, 1996, 1991, 1981; Uličný, 2004). The average thickness of sandflow strata reaches up to 5–8 cm from which a minimum dune height of 10 m can be inferred (Kocurek and Dott, 1981; Romain and Mountney, 2014) although this linear relationship has recently been proven not to be that straight-forward (Zhao et al., 2021). Nonetheless, some sets of cross-strata from the investigated sections are>10 m-thick (e.g., Fig. 7 or 8), which implies a much greater height of the dune. These dune height estimations fall into the range (10–20 m) of the seif and parabolic dunes marking the current topography of the Edel Land Peninsula (Fig. 1).

There is a predominance of the sandflow strata over the grainfall strata. Most of the preserved sandflow strata reach the base of the exposed unit that overlies paleosol horizons. Such extended sandflow strata are typical of aeolian dunes that had well-developed slipfaces during most of their periods of deposition, when sandflow processes were the main contributors to dune migration (Kocurek, 1991). It also characterises dune crestlines that were oriented transverse to prevailing effective palaeowinds (Jorgensen, 2012; Kocurek, 1991).

5.3. *Aeolian system geometry*

Apart of the differences in sediment composition and mode of origin, carbonate ramp and clastic systems produce very similar coastal sequences of deposits in response to analogous processes of dispersion, transport, and deposition (e.g., Evans, 1970). Therefore, the stack of landward-advancing dunes of the Tamala Limestone observable along the Zuytdorp Cliffs corresponds to a dry aeolian system with regional-scale interruptions of sedimentation (Jones et al., 2016). Because the red horizons separating aeolian sets of strata are heavily bioturbated (e.g., high density of rhizoliths) and do not present the typical features of wet interdunes, they constitute paleosols (Kocurek, 1988; Mountney, 2006a, 2006b) marking regional breaks in the aeolian accumulation. The thicknesses of the carbonate units and the size of the cross-strata indicate a high ratio of accumulation over downwind migration rates, which defines a field of great aggregation compared with a field of deflation (Mountney, 2011). In these settings, there is a significant

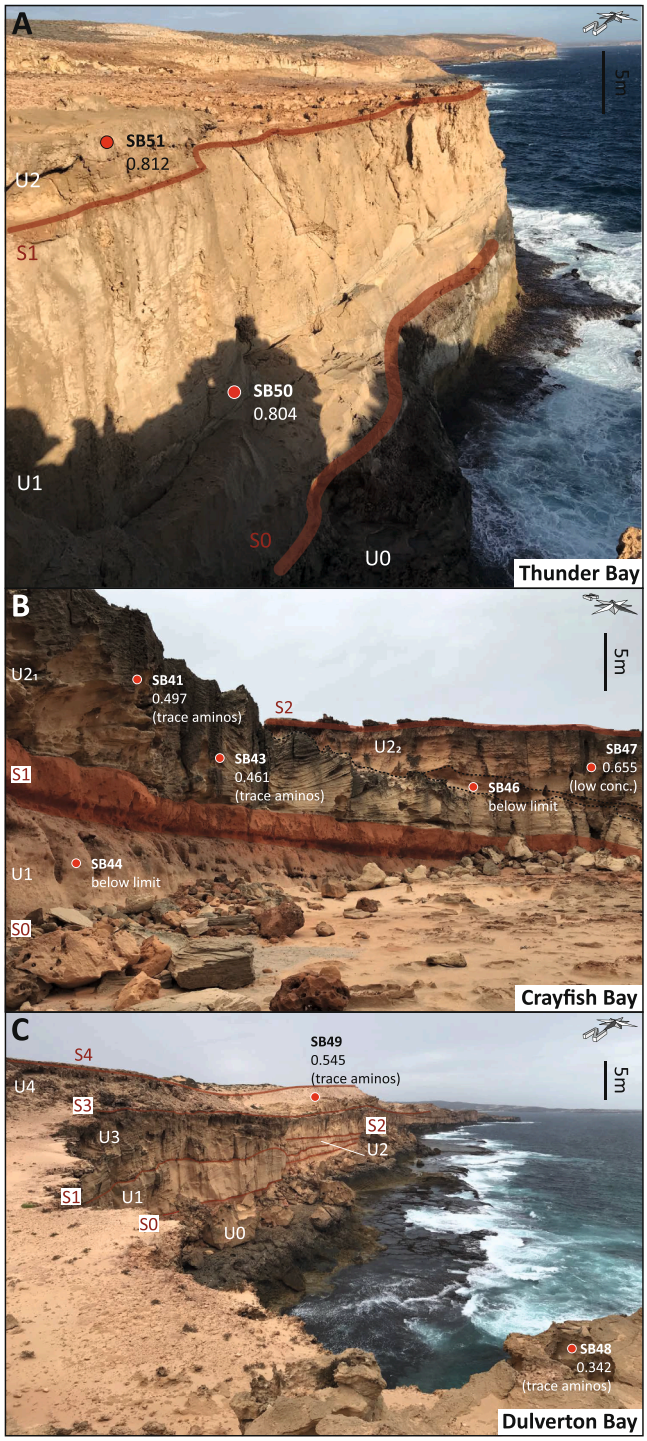

Fig. 14. Stratigraphy and A/I ratios of paleosol-capped aeolianites at three locations of the Zuytdorp Cliffs, from north to south: **A:** Thunder Bay; **B:** Crayfish Bay; and **C:** Dulverton Bay. A: A/I ratios show a problematic relative age inversion. B: All the collected samples showed trace, low concentrations, or concentrations of amino-acid below the detection limit. Two different A/I ratios were measured within the same Unit 2_1, which were both lower than the ratio measured in the overlapping Unit 2_2. C: Two samples retrieved within the same aeolianite (U4) showed only trace amino-acids that yielded to unmatching A/I ratios.

sediment supply and availability along with an accumulation process occurring via bedforms climbing over one another (Rubin and Hunter, 1982). The reactivation surfaces between two sub-units can form from the erosion of the dune slipface following a change of dune height, local

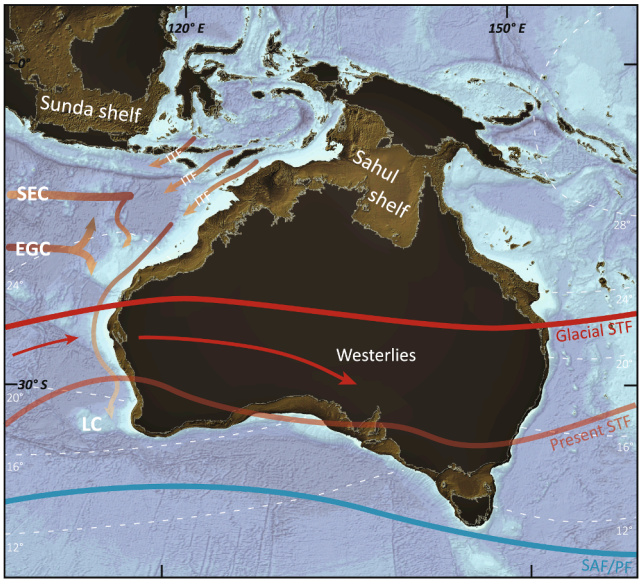

Fig. 15. Maximum extent of the exposed Sahul and Sunda shelves during the LGM (-120 m) and the associated prevailing atmospheric and oceanic circulation features. White dashed lines indicate the LGM mean annual SST estimated by Barrows and Juggins (2005). Note the shrinking of the IPWP to the north compared to its modern extent and position (Fig. 3). The shallowing of the Indonesian channels and straits led to a diminished transport of the IPWP waters by the ITF, which in turn led to a weakened LC (Petrick et al., 2019). This translates into less rainfall and a general aridification of Western Australia. The northward contraction and expansion of the Hadely and Ferrel cells, respectively, is illustrated by the migration north of both the STF and SAF/PF mean positions (Courtillat et al., 2020). Consequently, prevailing westerlies were blowing in the Shark Bay region.

wind direction and speed (e.g., reverse winds), or dune asymmetry (Kocurek, 1991; Mountney, 2006b; Rubin and Hunter, 1983).

5.4. Prevailing palaeowinds

The dominant planar geometry of the cross-strata, the prevailing sandflow strata, and the unimodal distribution of the cross-beds dip directions (Fig. 4-B) indicate landward-advancing (i.e., transgressive; Rowe and Bristow, 2015a, 2015b) dunes migrating sub-perpendicularly to the coast towards the NE. When looked at individually, the units defined for the four studied sections also show unimodal distributions of cross-strata orientations, which are interpreted as foresets. The evident dominant directions of effective palaeowinds are towards the NE and the E, with data being more or less widely distributed around these values. Only three units out of the 31 analysed indicate a NW palaeowind direction, with cross-strata dipping at high angles (~30°). They could either be correlated with reversing winds such as the ones blowing in winter at present, or interpreted as backslope dune deposits (i.e., backset sets).

5.5. Palaeoclimate and stratigraphic interpretations

The depositional timing of the Tamala Limestone remains an unsettled issue as of today (Hearty and O'Leary, 2008; Jorgensen, 2012; Lipar and Webb, 2014; Playford et al., 2013). The answer to the question of whether sediment accumulation occurred during interglacial or glacial periods is complicated by the lack of accuracy of the various dating methods and the alteration level of sediments. At present, the surface dunes from Carrarang Sand and the Denham Sand are mostly stabilised by vegetation despite the aridity of the region. The deposition of such considerable extensive dunes should have occurred during periods when sand transport was substantially facilitated. This implies a close

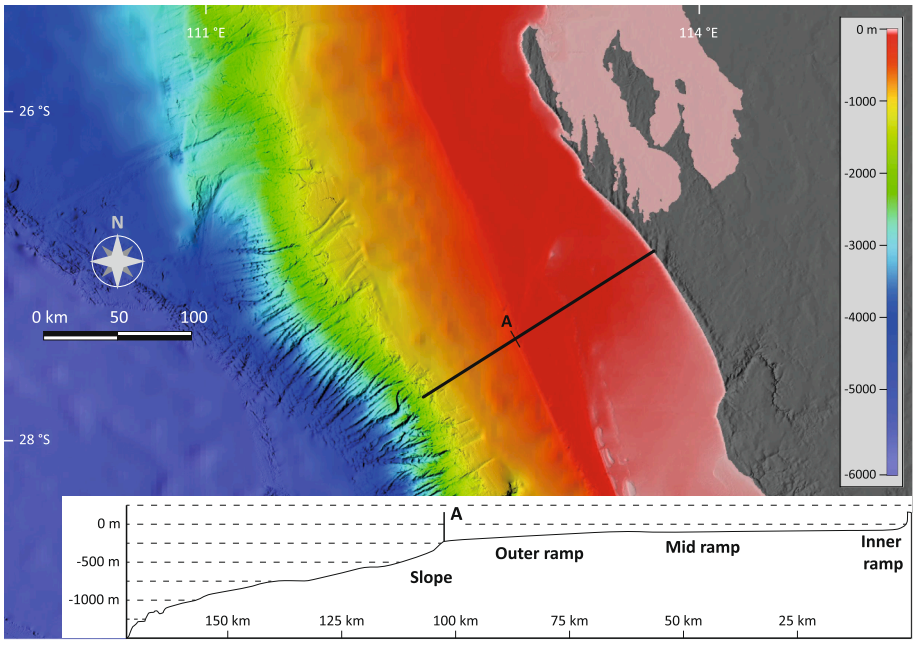

Fig. 16. Bathymetric map and cross-section showing the morphology of the extensive and gently-inclined Carnarvon Ramp (~100 km-long). According to James et al. (1999), the inner ramp is composed by the shallowest waters (0–50 m) and the Zuytdorp Cliffs; the mid-ramp (50–100 m) is an open sand plain showing the same sand composition than the Tamala Limestone aeolianites; the outer ramp and the slope (>100 m) produce very little carbonate sediment, mostly bivalves. A sea level drop of 120 m (e.g., LGM sea level fall) would expose about 80 km of the platform to wind action.

productive source of sediment (Pye and Tsoar, 2008), winds blowing above the saltation threshold (e.g., Fryberger and Dean, 1979; Kocurek and Lancaster, 1999), and a greater sediment availability, usually correlated with an increase in aridity likely causing a degradation of the vegetation cover.

During glacial periods, the decrease in sea surface temperature (SST) results in less evaporation above the Indo-Pacific Warm Pool (IPWP), which weakens the convection movement of the Hadley cell and induces the shrinking of the IPWP (Fig. 15), causing the northward retreat of its southern bound (Spooner et al., 2011). This would drastically reduce the southward transport of low salinity, warm IPWP waters by the Indonesian Throughflow (ITF; Barrows and Juggins, 2005; Martínez et al., 1999). This phenomenon is amplified by the cutting off and the substantial shallowing of the ITF channels caused by a lowered sea level resulting from an increase in continental ice volume (Petrick et al., 2019). An attenuation of the feeding ITF leads to a weakening of the Leeuwin Current (LC; Reeves et al., 2013), which translates into more arid conditions along Western Australia. Models for the Pliocene and LGM indicate a reduction in rainfall up to 30% when the ITF is considerably reduced (Di Nezio et al., 2016; DiNezio et al., 2018; Krebs et al., 2011). In summary, the LC is strong during interglacials and weak during glacials, which leads to humid and arid climate conditions, respectively. This glacial-interglacial pattern in Western Australia has been demonstrated for the past 500 ka, with enhanced aeolian transport during dry glacials and increased fluvial runoff during humid interglacials (Courtillat et al., 2020; Lipar et al., 2017; Petrick et al., 2019; Spooner et al., 2011; Stuut et al., 2014).

During the transition from a warm-humid interglacial to a cold-dry glacial, the Hadley and the Ferrel cells retreats/expands northward, respectively (Courtillat et al., 2020; De Deckker et al., 2012; Jiang et al., 2008, 2001; Jorgensen, 2012; Peterson, 1988; Scherer and Goldberg, 2007; Spooner et al., 2011; Uličný, 2004). This migration translates into a more northern position of the ITCZ, the Subtropical Front (STF), and both the Subantarctic Front (SAF)/Polar Front (PF) that are pushed closer to Australia by expanding Antarctic ice sheets (Fig. 15). It has already been shown for intervals of the Quaternary that this change in atmospheric circulation corresponds to an intensified aeolian transport (De Deckker et al., 2012; Courtillat et al., 2020). The enhanced influence of the westerlies in the Shark Bay region is shown by the palaeowind directions measured from the cross-strata and foresets orientations. This influence decreases towards the north with main wind vectors pointing more north at the Steep Point section (Fig. 5) than at the False Entrance Blowing Holes section (Fig. 8). Most of the studied units indicate dune migration from the west/south-west to east/north-east, which differs from the north–south orientation of the younger dunes presently lying at the surface and forming the Carrarang and Denham Sands (Le Guern, 2004). The few units showing structures dipping towards the north, north-west, and west could constitute preserved backsets, deposits linked with secondary airflow (Frank and Kocurek, 1996; Livingstone, 1986; Sweet and Kocurek, 1990; Tsoar, 1983; Walker, 1999; Walker and Nickling, 2002), or reflect the greater influence of the southeasterly trade winds of the Hadley cell in the region at the time (Jorgensen, 2012).

Carbonate sedimentation operates very differently on isolated, flat-topped rimmed platforms (e.g., the Bahamas) than on carbonate ramps (Burchette and Wright, 1992; Carew and Mylroie, 2001). Whilst sea level variations define the sediment production, sediment availably is controlled by climate (Abegg et al., 2001; Williams and Walkden, 2001). Generally, ramps show lower production rates and higher transport rates than flat-topped platforms (Sultana et al., 2021). The low-angle geometry of the extensive Carnarvon Ramp (~100 km; Fig. 16) makes the carbonate production very little sensitive to sea level variations but a large surface of sediment is exposed during sea level falls, making sediment available to wind transport. The aforementioned changes in oceanic and atmospheric circulation suggest a dry climate (i.e., weak LC) with strong westerlies blowing during glacial periods, when a significant amount of the platform is exposed (Fig. 17). On the contrary, interglacial periods are marked by a wet climate (i.e., strong LC) with weaker south winds blowing when a reduced amount of the platform is emerged. As such, sediment availability is drastically increased during glacials whilst sediment production remains constant. Therefore, it is unlikely that the Tamala Limestone dunes were deposited during interglacials and paleosols formed during glacials as previously suggested by some authors (Hearty and O'Leary, 2008; Lipar and Webb, 2014). It is even less likely for the MIS 5, MIS 7, and MIS 11, during which the LC was stronger than today so that climate was more humid, which would have increased the vegetation cover and limited dune mobility (Hope, 1994; Markgraf et al., 1992; Spooner et al., 2011; van der Kaars and De Deckker, 2003, 2002). The in-situ nature of the siliciclastic components of paleosol horizons (Bastian, 2010, 1996, 1994;

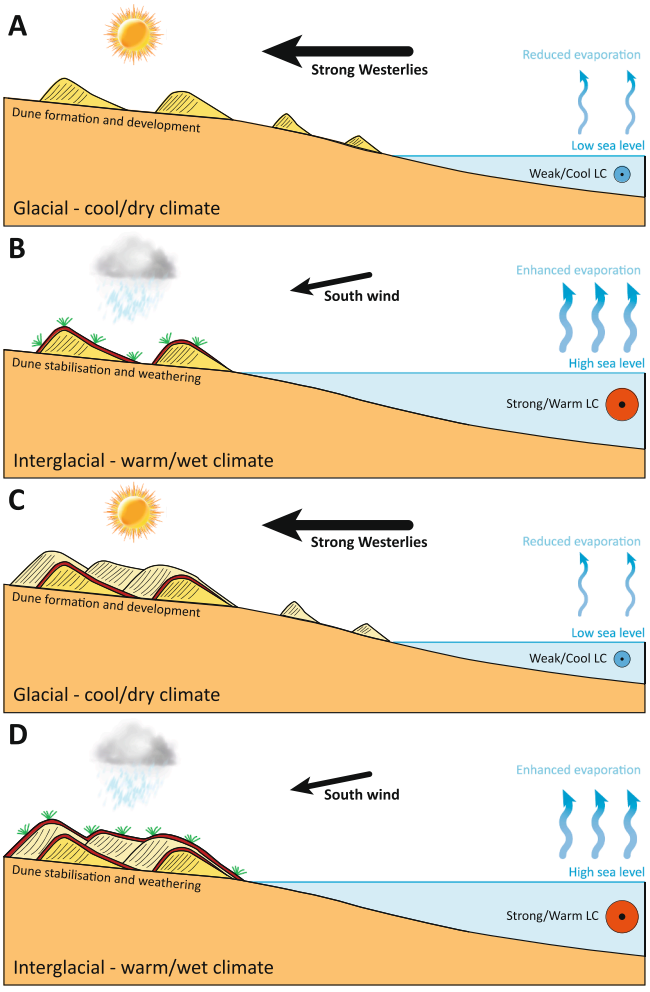

Fig. 17. Schematic cross-section illustrating the depositional model for the Tamala Limestone aeolianites in the Shark Bay region. During glacial periods, a large surface of the platform is exposed to wind action, allowing aeolian transport of sediments. The LC is weak and cool, leading to reduced evaporation rates, and ultimately to a dry climate. The northward migration of the Hadley and Ferrel cells brings strong westerlies in the region, allowing formation and development of aeolianites. Carbonate production takes place during periods of high sea level (i.e., interglacias), when the Carnarvon Ramp is flooded and sea water is warm. The strong and warm Leeuwin Current (LC) causes the climate to be wet through high evaporation rates. Dune stabilisation and weathering occurs during this stage. Wind pattern is similar to the present one with winds blowing from the south in average, which is inconsistent with sedimentary structures orientation measured in the Tamala Limestone aeolianites. Modified after (Assal et al., 2020).

Newsome, 2000; Playford et al., 2013; Tapsell et al., 2003) indicates a greater dissolution of the carbonate caused by intensified rainfall, correlating with interglacial periods. Moreover, the Tamala Limestone as exposed at the Zuytdorp Cliffs is very similar to a dry aeolian system, correlating periods of deposition with glacials. A high rate of accumulation is represented by the thicknesses of the cross-strata sets, which implies a close, profusive source of sediment and high transport rates. Such glacial aeolian systems linked with carbonate ramps have been described both in the Mesozoic (Abegg and Handford, 2001; Dodd et al., 2001) and in the Cenozoic (Zhou et al., 1994). In other places such as the northwestern coast of Egypt, coastal aeolianites connected to a carbonate ramp system have been building during interglacial periods that corresponded to arid periods (Assal et al., 2020), reinforcing the notion that different climate settings and platform geometries lead to different periods of deposition.

Overall, it seems that most of the Tamala Limestone has been deposited under westerly winds prevailing in the region after a northward migration of the subtropical highs (Denton et al., 2010; Kohfeld et al., 2013). Whilst these highs seasonally bring rainfall in austral winter during their northern displacement, the long-term trend during dry glacials suggests moisture levels were not high enough to prevent dune mobilisation.

6. Conclusion

The Tamala Limestone currently exposed along the Zuytdorp Cliffs, in the Shark Bay region, shows cyclic deposition of coastal aeolianites alternating with breaks in sedimentation represented by paleosols. The regional amino acid racemization survey coupled with a stratigraphic and sedimentological analysis, based on 3D models of the cliffs, provide new insight into the depositional timing of the Tamala Limestone aeolianites relative to glacial/interglacial cycles and the climate conditions at the time. The decrease in both A/I values and amino acid concentrations from inland units and stratigraphically lower units at the Zuytdorp Cliffs indicates a more advanced diagenetic state correlating with an aging of the units. This indicates an inland migration of sediments taking their source on the shore.

The Tamala Limestone is primarily constituted by landward-advancing dunes (i.e., transverse) migrating parallel to the prevailing winds. The stratigraphic layout displayed along the western coast of Edel Land Peninsula is very similar to the one form by a dry accumulating siliciclastic aeolian system (i.e., no interdune deposits) with an important accumulation rate with respect to the downwind migration rate.

All these observations strongly suggest that the aeolian accumulation in the Shark Bay region occurred during dry/cold glacials. Lower sea levels would have exposed a consequent surface of the Carnarvon carbonate ramp where significant quantities of sediment would have been prone to transport by wind. Expanding ice sheets induced sea level drops which, coupled with lowered SST of the IPWP, would have cut off the ITF resulting in a substantially weakened LC. Consequently, diminished rainfall and moisture would have contributed to the arid climate during glacial periods. The influence of westerlies during the dunes deposition compared to today's wind regimes correlates with northward migration of both the Hadley and Ferrel cells.

Further studies to accurately date the successive units along the Zuytdorp Cliffs are warranted in order to properly constrain palaeoclimate and atmospheric circulation associated with the deposition of aeolianites in this peculiar region.

CRediT authorship contribution statement

Lucas Vimpere: Conceptualization, Methodology, Formal analysis, Investigation, Resources, Writing – original draft, Writing – review & editing, Visualization, Supervision, Project administration. **Nicolò Del Piero:** Investigation. **Aymeric Le Cotonnec:** Formal analysis, Writing – original draft. **Pascal Kindler:** Funding acquisition, Writing – review & editing. **Sébastien Castelltort:** Funding acquisition, Writing – review & editing.

Declaration of Competing Interest

The authors declare that they have no known competing financial interests or personal relationships that could have appeared to influence the work reported in this paper.

Acknowledgements

This project was funded by the Department of Earth Sciences of the University of Geneva. Our gratitude goes to the Earth Observation Centre at the German Aerospace Centre (DLR) for generously providing

the DEMs needed. We would like to acknowledge the Amino Acid Geochronology Lab of the Northern Arizona University for their efficiency and for remaining available to discuss the results. We convey our warm thanks to Dave, the Chief Ranger of Cervantes who made us discover the splendid Pinnacles Desert. Dr Stephen E. Watkins greatly improved the manuscript with very valuable comments and review.

Appendix

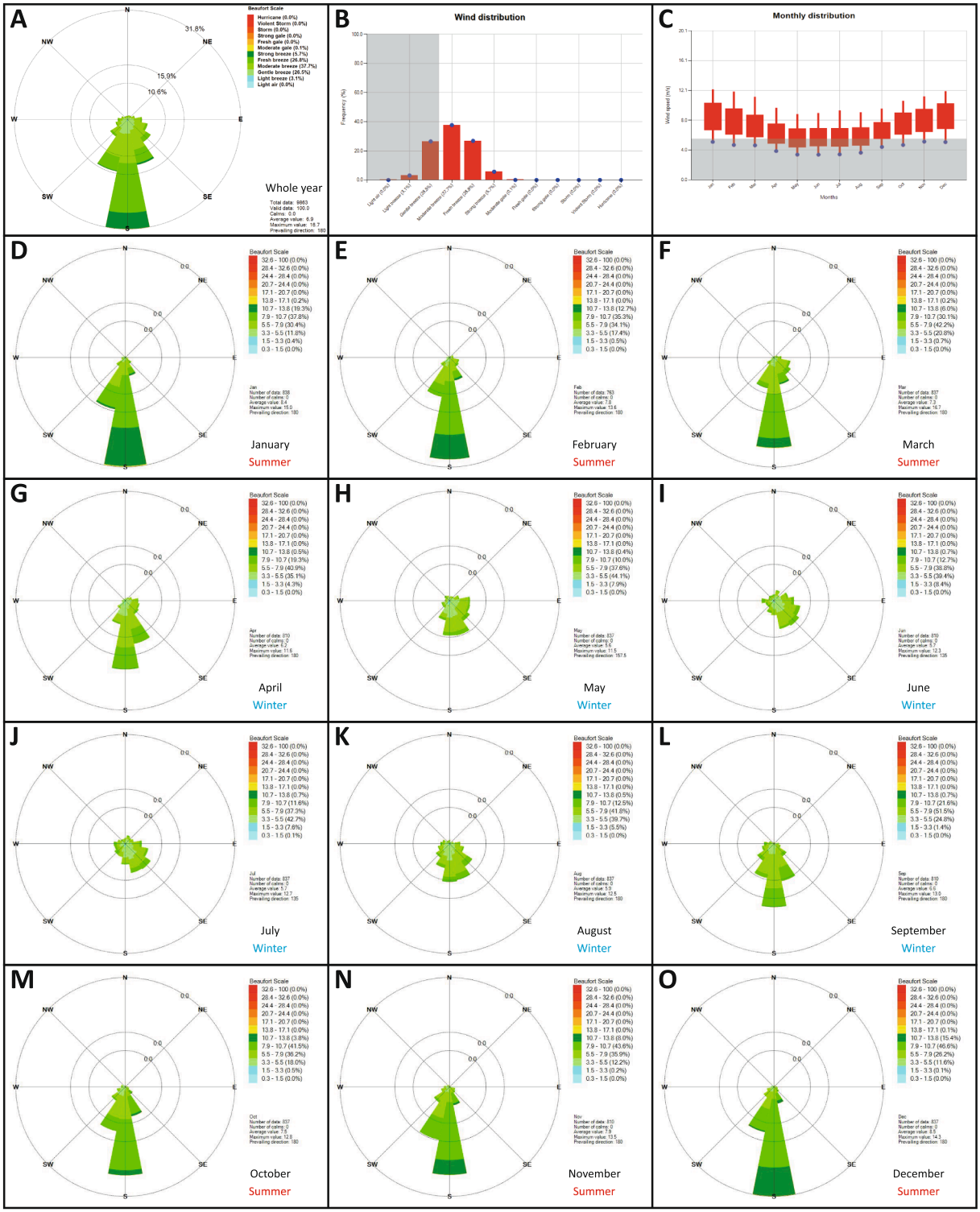

Appendix A. Annual wind frequency rose (**A**); wind speed annual (**B**) and monthly distribution (**C**) and at False Entrance. The greyed zones represent the threshold velocity of wind from which sand transport is initiated (Fryberger and Dean, 1979). D to O show the monthly wind frequency roses. All the graphs were generated based on daily-averaged (from 1990 to 2017) wind speed and direction data collected from the Power-8 NOAA database (Stackhouse et al., 2018).

References

Abegg, F., Handford, C., 2001. Deflation Origin of Mississippian Carbonate Eolianites. Modern and Ancient Carbonate Eolianites: Sedimentology, Sequence Stratigraphy. and Diagenesis, SEPM Special Publication, Southwestern Kansas, U.S.A.

Abegg, F., Loope, D., Harris, P., 2001. Carbonate eolianites—Depositional models and diagenesis, in: Modern and Ancient Carbonate Eolianites: Sedimentology, Sequence Stratigraphy, and Diagenesis, SEPM Special Publication.

Assal, E.M., Abdel-Fattah, Z.A., El-Asmar, H.M., 2020. Facies architecture and controlling factors induced depositional model of the Quaternary carbonate eolianites in the northwestern Mediterranean coast of Egypt. Int. J. Earth Sci. 109 (5), 1659–1682. https://doi.org/10.1007/s00531-020-01863-3.

Barrows, T.T., Juggins, S., 2005. Sea-surface temperatures around the Australian margin and Indian Ocean during the Last Glacial Maximum. Quat. Sci. Rev. 24 (7-9), 1017–1047. https://doi.org/10.1016/j.quascirev.2004.07.020.

Bastian, L.V., 2010. Comment on Hearty, P.J. and O•Leary, M.J., 2008. Carbonate eolianites, quartz sands, and Quaternary sea-level cycles, Western Australia: A chronostratigraphic approach. Quaternary Geochronology 3: 26–55. Quat. Geochronol. 5 (1), 76–77.

Bastian, L.V., 1996. Residual soil mineralogy and dune subdivision, Swan Coastal Plain. Western Australia. Aust. J. Earth Sci. 43 (1), 31–44. https://doi.org/10.1080/08120099608728233.

Bastian, L.V., 1994. The dune systems of the Swan Coastal Plain: subdivision based on mineral trends in the surface soils. Chemistry Centre of WA.

Belknapt, D.F., Mart, Y., 2021. Sea-Level Lowstand in the Eastern Mediterranean: Late Pleistocene Coastal Terraces Offshore Northern Israel. J. Coast. Res. 15, 399–412.

Brooke, B., 2001. The distribution of carbonate eolianite. Earth-Sci. Rev. 55 (1-2), 135–164. https://doi.org/10.1016/S0012-8252(01)00054-X.

Burchette, T.P., Wright, V.P., 1992. Carbonate ramp depositional systems. Sediment. Geol. 79 (1-4), 3–57. https://doi.org/10.1016/0037-0738(92)90003-A.

Cai, W., Santoso, A., Wang, G., Weller, E., Wu, L., Ashok, K., Masumoto, Y., Yamagata, T., 2014. Increased frequency of extreme Indian Ocean Dipole events due to greenhouse warming. Nature 510 (7504), 254–258. https://doi.org/10.1038/nature13327.

Carew, J.L., Mylroie, J.E., 2001. Quaternary Carbonate Eolianites of the Bahamas: Useful Analogues for the Interpretation of Ancient Rocks?, in: Abegg, F.E. (Rick), Loope, D. B., Harris, P.M. (Mitch) (Eds.), Modern and Ancient Carbonate Eolianites: Sedimentology, Sequence Stratigraphy, and Diagenesis, SEPM Special Publication. SEPM Society for Sedimentary Geology, p. 0. 10.2110/pec.01.71.0033.

Courtillat, M., Hallenberger, M., Bassetti, M.-A., Aubert, D., Jeandel, C., Reuning, L., Korpanty, C., Moissette, P., Mounic, S., Saavedra-Pellitero, M., 2020. New Record of Dust Input and Provenance During Glacial Periods in Western Australia Shelf (IODP Expedition 356, Site U1461) from the Middle to Late Pleistocene. Atmosphere 11, 1251. https://doi.org/10.3390/atmos11111251.

Current, S.E., Current, C., Strait, S., Passage, T., Current, E.G., 1996. The WOCE Indonesian Throughflow Repeat Hydrography Sections: I10 and IR6. Int. WOCE Newsl. 44.

De Deckker, P., 2016. The Indo-Pacific Warm Pool: critical to world oceanography and world climate. Geosci. Lett. 3, 20. https://doi.org/10.1186/s40562-016-0054-3.

De Deckker, P., Moros, M., Perner, K., Jansen, E., 2012. Influence of the tropics and southern westerlies on glacial interhemispheric asymmetry. Nat. Geosci. 5 (4), 266–269. https://doi.org/10.1038/ngeo1431.

Denton, G.H., Anderson, R.F., Toggweiler, J.R., Edwards, R.L., Schaefer, J.M., Putnam, A. E., 2010. The last glacial termination. Science 328 (5986), 1652–1656.

Di Nezio, P.N., Timmermann, A., Tierney, J.E., Jin, F.-F., Otto-Bliesner, B., Rosenbloom, N., Mapes, B., Neale, R., Ivanovic, R.F., Montenegro, A., 2016. The climate response of the Indo-Pacific warm pool to glacial sea level. Paleoceanography 31 (6), 866–894. https://doi.org/10.1002/2015PA002890.

DiNezio, P.N., Tierney, J.E., Otto-Bliesner, B.L., Timmermann, A., Bhattacharya, T., Rosenbloom, N., Brady, E., 2018. Glacial changes in tropical climate amplified by the Indian Ocean. Sci, Adv, p. 12.

Dodd, J., Hunter, R., Merkley, P., 2001. Eolianite-bearing depositional cycles in the Ste. Genevieve Limestone of Indiana and Kentucky: evidence for Mississippian eustasy., in: Abegg, F., Harris, P., Loope, D. (Eds.), Modern and Ancient Carbonate Eolianites: Sedimentology, Sequence Stratigraphy, and Diagenesis, SEPM Special Publication. pp. 151–166.

Engelmann, A., Neber, A., Frechen, M., Wolfgang Boenigk, Ronen, A., 2001. Luminescence chronology of Upper Pleistocene and Holocene aeolianites from Netanya South - Sharon Coastal Plain. Quaternary Science Reviews 20 (5-9), 799–804.

Evans, G., 1970. Coastal and nearshore sedimentation: A comparison of clastic and carbonate deposition. Proc. Geol. Assoc. 81 (3), 493–508. https://doi.org/10.1016/S0016-7878(70)80010-4.

Fornós, J., Clemmensen, L., Gómez-Pujol, L., Ginés, A., Ginés, J., 2012. Pleistocene eolianites and low sea levels. In: Ginés, A. (Ed.), Mallorca: A Mediterranean Benchmark for Quaternary Studies. Societat d'Història Natural de les Balears, Palma de Mallorca, pp. 85–110.

Frank, A., Kocurek, G., 1996. Toward a model for airflow on the lee side of aeolian dunes. Sedimentology 43 (3), 451–458. https://doi.org/10.1046/j.1365-3091.1996.d01-20.x.

Frechen, M., Dermann, B., Boenigk, W., Ronen, A., 2001. Luminescence chronology of aeolianites from the section at Givat Olga - Coastal Plain of Israel. Quat. Sci. Rev. 20 (5-9), 805–809.

Fryberger, S., Dean, G., 1979. Dune forms and wind regime, in: A Study of Global Sand Seas. US Government Printing Office Washington, pp. 137–169.

Fumanal, M., 1995. Pleistocene dune systems in the Valencian Betic cliffs (Spain). INQUA Subcomission Mediterr. Black Sea Shorel. Newsl. 17, 32–38.

Godfrey, J.S., Ridgway, K.R., 1985. The large-scale environment of the poleward-flowing Leeuwin Current, Western Australia: longshore steric height gradients, wind stresses and geostrophic flow. J. Phys. Oceanogr. 15 (5), 481–495.

Gordon, A.L., Fine, R.A., 1996. Pathways of water between the Pacific and Indian oceans in the Indonesian seas. Nature 379 (6561), 146–149. https://doi.org/10.1038/379146a0.

Hearty, P.J., Kaufman, D.S., 2009. A Cerion-based chronostratigraphy and age model from the central Bahama Islands: Amino acid racemization and 14C in land snails and sediments. Quat. Geochronol. 4 (2), 148–159. https://doi.org/10.1016/j.quageo.2008.08.002.

Hearty, P.J., Kaufman, D.S., 2000. Whole-Rock Aminostratigraphy and Quaternary Sea-Level History of the Bahamas. Quat. Res. 54 (2), 163–173. https://doi.org/10.1006/qres.2000.2164.

Hearty, P.J., O'Leary, M.J., 2008. Carbonate eolianites, quartz sands, and Quaternary sea-level cycles, Western Australia: A chronostratigraphic approach. Quat. Geochronol. 3 (1-2), 26–55. https://doi.org/10.1016/j.quageo.2007.10.001.

Hunter, R.E., 1977. Basic types of stratification in small eolian dunes. Sedimentology 24 (3), 361–387.

James, N.P., Collins, L.B., Bone, Y., Hallock, P., 1999. Subtropical carbonates in a temperate realm: modern sediments on the southwest Australian shelf. J. Sediment. Res. 69 (6), 1297–1321.

Jiang, X., Pan, Z., Fu, Q., 2001. Regularity of paleowind directions of the Early Cretaceous Desert in Ordos Basin and climatic significance. Sci. China Ser. Earth Sci. 44 (1), 24–33. https://doi.org/10.1007/BF02906882.

Jiang, X., Pan, Z., Xu, J., Li, X., Xie, G., Xiao, Z., 2008. Late Cretaceous aeolian dunes and reconstruction of palaeo-wind belts of the Xinjiang Basin, Jiangxi Province. China. Palaeogeogr. Palaeoclimatol. Palaeoecol. 257 (1-2), 58–66. https://doi.org/10.1016/j.palaeo.2007.09.012.

Jones, F.H., dos Scherer, C.M., S., Kuchle, J.,, 2016. Facies architecture and stratigraphic evolution of aeolian dune and interdune deposits, Permian Caldeirão Member (Santa Brígida Formation). Brazil. Sediment. Geol. 337, 133–150. https://doi.org/10.1016/j.sedgeo.2016.03.018.

Jorgensen, D., 2012. Quaternary stratigraphy, palaeowinds and palaeoenvironments of carbonate aeolianite on the Garden Island Ridge and in the Naturaliste-Leeuwin region, southwest Western Australia. James Cook University, Townsville. PhD Thesis.

Kaufman, D.S., Manley, W.F., 1998. A new procedure for determining DL amino acid ratios in fossils using reverse phase liquid chromatography. Quat. Sci. Rev. 17 (11), 987–1000.

Kilibarda, Z., Kilibarda, V., 2016. Seasonal geomorphic processes and rates of sand movement at Mount Baldy dune in Indiana, USA. Aeolian Res. 23, 103–114. https://doi.org/10.1016/j.aeolia.2016.10.004.

Kocurek, G., 1996. Desert aeolian systems. In: Reading, H.G. (Ed.), Sedimentary Environments: Processes, Facies and Stratigraphy. Blackwell Science, Oxford, pp. 125–153.

Kocurek, G., 1991. Interpretation of ancient eolian sand dunes. Annu. Rev. Earth Planet. Sci. 19 (1), 43–75.

Kocurek, G., 1988. First-order and super bounding surfaces in eolian sequences—Bounding surfaces revisited. Sediment. Geol. 56 (1-4), 193–206. https://doi.org/10.1016/0037-0738(88)90054-1.

Kocurek, GARY, 1981. Significance of interdune deposits and bounding surfaces in aeolian dune sands. Sedimentology 28 (6), 753–780.

Kocurek, G., Dott, R., 1981. Distinctions and uses of stratification types in the interpretation of eolian sand. J. Sediment. Res. 51.

Kocurek, G., Lancaster, N., 1999. Aeolian system sediment state: theory and Mojave Desert Kelso dune field example. Sedimentology 46 (3), 505–515. https://doi.org/10.1046/j.1365-3091.1999.00227.x.

Kohfeld, K.E., Graham, R.M., de Boer, A.M., Sime, L.C., Wolff, E.W., Le Quéré, C., Bopp, L., 2013. Southern Hemisphere westerly wind changes during the Last Glacial Maximum: paleo-data synthesis. Quat. Sci. Rev. 68, 76–95. https://doi.org/10.1016/j.quascirev.2013.01.017.

Krebs, U., Park, W., Schneider, B., 2011. Pliocene aridification of Australia caused by tectonically induced weakening of the Indonesian throughflow. Palaeogeogr. Palaeoclimatol. Palaeoecol. 309 (1-2), 111–117. https://doi.org/10.1016/j.palaeo.2011.06.002.

Le Guern, P., 2004. Caractérisation pétrographique et pétrotexturale des éolianites holocènes et pléistocènes. University of Geneva, Geneva.

Lipar, M., Webb, J.A., 2014. Middle–late Pleistocene and Holocene chronostratigraphy and climate history of the Tamala Limestone, Cooloongup and Safety Bay Sands, Nambung National Park, southwestern Western Australia. Aust. J. Earth Sci. 61 (8), 1023–1039. https://doi.org/10.1080/08120099.2014.966322.

Lipar, M., Webb, J.A., Cupper, M.L., Wang, N., 2017. Aeolianite, calcrete/microbialite and karst in southwestern Australia as indicators of Middle to Late Quaternary palaeoclimates. Palaeogeogr. Palaeoclimatol. Palaeoecol. 470, 11–29. https://doi.org/10.1016/j.palaeo.2016.12.019.

Lisiecki, L.E., Raymo, M.E., 2005. A Pliocene-Pleistocene stack of 57 globally distributed benthic δ 18O records. Paleoceanography 20 (1), n/a–n/a. https://doi.org/10.1029/2004PA001071.

Livingstone, I., 1986. Geomorphological significance of wind flow patterns over a Namib linear dune, in: Nickling, W. (Ed.), Aeolian Geomorphology. pp. 97–112.

Markgraf, V., Dodson, J.R., Kershaw, A.P., McGlone, M.S., Nicholls, N., 1992. Evolution of late pleistocene and holocene climates in the circum-south pacific land areas. Clim. Dyn. 6 (3-4), 193–211. https://doi.org/10.1007/BF00193532.

Martínez, J.I., De Deckker, P., Barrows, T.T., 1999. Palaeoceanography of the last glacial maximum in the eastern Indian Ocean: planktonic foraminiferal evidence.

Palaeogeogr. Palaeoclimatol. Palaeoecol. 147 (1-2), 73–99. https://doi.org/10.1016/S0031-0182(98)00153-9.
McBride, J., 1987. The Australian summer monsoon. Monsoon Meteorol. 203, 13.
Mountney, N.P., 2006a. Mountney, N. P., Posamentier, H. W., & Walker, R. G. (2006). Eolian facies models. Special Publication-Sepm, 84, 19., in: Walker, R.G., Posamentier, H. (Eds.), Facies Models Revisited, SEPM Special Publication. Oklahoma, pp. 19–83.
Mountney, N.P., 2006b. Periodic accumulation and destruction of aeolian erg sequences in the Permian Cedar Mesa Sandstone, White Canyon, southern Utah, USA. Sedimentology 53 (4), 789–823. https://doi.org/10.1111/j.1365-3091.2006.00793.x.
Newsome, D., 2000. Origin of sandplains in Western Australia: A review of the debate and some recent findings. Aust. J. Earth Sci. 47 (4), 695–706.
Peterson, F., 1988. Pennsylvanian to Jurassic eolian transportation systems in the western United States. Sediment. Geol. 56 (1-4), 207–260. https://doi.org/10.1016/0037-0738(88)90055-3.
Petrick, B., Martínez-García, A., Auer, G., Reuning, L., Auderset, A., Deik, H., Takayanagi, H., De Vleeschouwer, D., Iryu, Y., Haug, G.H., 2019. Glacial Indonesian Throughflow weakening across the Mid-Pleistocene Climatic Transition. Sci. Rep. 9, 16995. https://doi.org/10.1038/s41598-019-53382-0.
Pietsch, T., Olley, J., 2005a. Report on the optical dating of sediment samples from Perth and Womerangee, supplied by Brendan Brooke [collected by P Haines and B Brook]: Report to Geoscience Australia and the Geological Survey of Western Australia (unpublished).
Pietsch, T., Olley, J., 2005. Report on the optical dating of sediment samples from Rottnest Island, supplied by Brendan Brooke [collected by P Haines and PE Playford]. Report to Geoscience Australia and the Geological Survey of Western Australia (unpublished).
Playford, P., 2003. Quaternary tectonism in the Carnarvon Basin, Western Australia. Tectonics and Structural Geology Field Meeting, Kalbarri, Western Australia, Presented at the Specialist Group, p. 89.
Playford, P., Cockbain, A., Berry, P., Robderts, A., Haines, P., Brooke, B., Geological Survey of Western Australia, 2013. The geology of Shark Bay.
Playford, P.E., Cockbain, A., Lowe, G.H., 1976. Geology of the Perth Basin. West. Aust. Geol. Surv. Bull. 124, 311.
Porat, N., Wintle, A., 1995. IRSL dating of aeolianites from the late Pleistocene coastal Kurkar ridge. Israel, Presented at the NQUA XIV, Berlin.
Price, D., Brooke, B., Woodroffe, C., 2001. Thermoluminescence dating of aeolianites from Lord Howe Island and South-West Western Australian. Quat. Sci. Rev. 6.
Pye, K., Tsoar, H., 2008. Aeolian sand and sand dunes. Springer Science & Business Media.
Reeves, J.M., Bostock, H.C., Ayliffe, L.K., Barrows, T.T., De Deckker, P., Devriendt, L.S., Dunbar, G.B., Drysdale, R.N., Fitzsimmons, K.E., Gagan, M.K., Griffiths, M.L., Haberle, S.G., Jansen, J.D., Krause, C., Lewis, S., McGregor, H.V., Mooney, S.D., Moss, P., Nanson, G.C., Purcell, A., van der Kaars, S., 2013. Palaeoenvironmental change in tropical Australasia over the last 30,000 years – a synthesis by the OZ-INTIMATE group. Quat. Sci. Rev. 74, 97–114. https://doi.org/10.1016/j.quascirev.2012.11.027.
Romain, H.G., Mountney, N.P., 2014. Reconstruction of three-dimensional eolian dune architecture from one-dimensional core data through adoption of analog data from outcrop. AAPG Bull. 98, 1–22. https://doi.org/10.1306/05201312109.
Roof, S., 1997. Comparison of isoleucine epimerization and leaching potential in the molluskan genera Astarte, Macoma, and Mya. Geochim. Cosmochim. Acta 61, 5325–5333. https://doi.org/10.1016/S0016-7037(97)00294-9.
Rowe, M., Bristow, C., 2015a. Sea-level controls on carbonate beaches and coastal dunes (eolianite): Lessons from Pleistocene Bermuda. Geol. Soc. Am. Bull. 127, 1645–1665. https://doi.org/10.1130/B31237.1.
Rowe, M., Bristow, C.S., 2015b. Landward-advancing Quaternary eolianites of Bermuda. Aeolian Res. 19, 235–249. https://doi.org/10.1016/j.aeolia.2015.06.007.
Rubin, D., Hunter, R., 1983. Reconstructing bedform assemblages from compound crossbedding. Developments in Sedimentology. 407–427.
Rubin, D., Hunter, R., 1982. Bedform climbing in theory and nature. Sedimentology 29, 121–138.
Saji, N.H., Goswami, B.N., Vinayachandran, P.N., Yamagata, T., 1999. A dipole mode in the tropical Indian Ocean. Nature 401, 360–363. https://doi.org/10.1038/43854.
Scherer, C.M.S., Goldberg, K., 2007. Palaeowind patterns during the latest Jurassic–earliest Cretaceous in Gondwana: Evidence from aeolian cross-strata of the Botucatu Formation. Brazil. Palaeogeogr. Palaeoclimatol. Palaeoecol. 250, 89–100. https://doi.org/10.1016/j.palaeo.2007.02.018.
Smith, A., Massuel, S., Pollock, D., 2011. Geohydrology of the Tamala Limestone Formation in the Perth region: origin and role of secondary porosity. CSIRO Water Healthy Ctry. Natl. Res. Flagship 74.
Spooner, M.I., Barrows, T.T., De Deckker, P., Paterne, M., 2005. Palaeoceanography of the Banda Sea, and Late Pleistocene initiation of the Northwest Monsoon. Glob. Planet. Change 49, 28–46. https://doi.org/10.1016/j.gloplacha.2005.05.002.
Spooner, M.I., De Deckker, P., Barrows, T.T., Fifield, L.K., 2011. The behaviour of the Leeuwin Current offshore NW Australia during the last five glacial–interglacial cycles. Glob. Planet. Change 75, 119–132. https://doi.org/10.1016/j.gloplacha.2010.10.015.
Stackhouse, P., Zhang, T., Westberg, D., Barnett, A., Bristow, T., Macpherson, B., Hoell, J., 2018. POWER Release 8 (with GIS Applications) Methodology (Data Parameters, Sources, and Validation—Data Version 8.0. 1). NASA Langley Research Center, Hampton, VA, USA.
Stuut, J.-B.-W., Temmesfeld, F., De Deckker, P., 2014. A 550 ka record of aeolian activity near North West Cape, Australia: inferences from grain-size distributions and bulk chemistry of SE Indian Ocean deep-sea sediments. Quat. Sci. Rev. 83, 83–94. https://doi.org/10.1016/j.quascirev.2013.11.003.
Sultana, D., Burgess, P., Bosence, D., 2021. How do carbonate factories influence carbonate platform morphology? Exploring production-transport interactions with numerical forward modelling. Sedimentology sed.12943. 10.1111/sed.12943.
Suppiah, R., 1992. The Australian summer monsoon: a review. Prog. Phys. Geogr. Earth Environ. 16, 283–318. https://doi.org/10.1177/030913339201600302.
Sweet, M.L., Kocurek, G., 1990. An empirical model of aeolian dune lee-face airflow. Sedimentology 37, 1023–1038. https://doi.org/10.1111/j.1365-3091.1990.tb01843.x.
Tapsell, P., Newsome, D., Bastian, L., 2003. Origin of yellow sand from Tamala Limestone on the Swan Coastal Plain. Western Australia. Aust. J. Earth Sci. 50, 331–342.
Tomczak, M., Godfrey, J.S., 2003. Regional oceanography: an introduction. Daya Books.
Tsoar, H., 1983. Dynamic processes acting on a longitudinal (seif) sand dune. Sedimentology 30, 567–578. https://doi.org/10.1111/j.1365-3091.1983.tb00694.x.
Uličný, D., 2004. A drying-upward aeolian system of the Bohdašín Formation (Early Triassic), Sudetes of NE Czech Republic: record of seasonality and long-term palaeoclimate change. Sediment. Geol. 167, 17–39. https://doi.org/10.1016/j.sedgeo.2004.01.014.
van der Kaars, S., De Deckker, P., 2003. Pollen distribution in marine surface sediments offshore Western Australia. Rev. Palaeobot. Palynol. 124, 113–129. https://doi.org/10.1016/S0034-6667(02)00250-6.
van der Kaars, S., De Deckker, P., 2002. A Late Quaternary pollen record from deep-sea core Fr10/95, GC17 offshore Cape Range Peninsula, northwestern Western Australia. Rev. Palaeobot. Palynol. 120, 17–39. https://doi.org/10.1016/S0034-6667(02)00075-1.
Wakelin-King, G.A., Webb, J.A., 2020. Origin, geomorphology and geoheritage potential of Australia's longest coastal cliff lines. Aust. J. Earth Sci. 67, 649–661. https://doi.org/10.1080/08120099.2020.1742202.
Walker, I.J., 1999. Secondary airflow and sediment transport in the lee of a reversing dune 12.
Walker, I.J., Nickling, W.G., 2002. Dynamics of secondary airflow and sediment transport over and in the lee of transverse dunes. Prog. Phys. Geogr. Earth Environ. 26, 47–75. https://doi.org/10.1191/0309133302 pp325ra.
Webster, P.J., Moore, A.M., Loschnigg, J.P., Leben, R.R., 1999. Coupled ocean–atmosphere dynamics in the Indian Ocean during 1997–98. Nature 401, 356–360. https://doi.org/10.1038/43848.
Wessel, B., Huber, M., Wohlfart, C., Marschalk, U., Kosmann, D., Roth, A., 2018. Accuracy assessment of the global TanDEM-X Digital Elevation Model with GPS data. ISPRS J. Photogramm. Remote Sens. 139, 171–182. https://doi.org/10.1016/j.isprsjprs.2018.02.017.
Whitacre, K., Kaufman, D., Kosnik, M., Hearty, P., 2017. Converting A/I values (ion exchange) to D/L values (reverse phase) for amino acid geochronology. Quat. Geochronol. 37, 1–6. https://doi.org/10.1016/j.quageo.2016.10.004.
Wijffels, S., Sprintall, J., Fieux, M., Bray, N., 2002. The JADE and WOCE I10/IR6 Throughflow sections in the southeast Indian Ocean. Part 1: water mass distribution and variability. Deep Sea Res. Part II Top. Stud. Oceanogr. 49, 1341–1362. https://doi.org/10.1016/S0967-0645(01)00155-2.
Williams, A.H., Walkden, G., 2001. Carbonate eolianites from a eustatically influenced ramp-like setting: the Quaternary of the southern Arabian Gulf. Modern and Ancient Carbonate Eolianites: Sedimentology, Sequence Stratigraphy. and Diagenesis, SEPM Special Publication.
Yan, X.-H., Ho, C.-R., Zheng, Q., Klemas, V., 1992. Temperature and Size Variabilities of the Western Pacific Warm Pool. Science 258, 1643–1645. https://doi.org/10.1126/science.258.5088.1643.
Zhao, F., Cardenas, B.T., Kim, W., 2021. Controls of aeolian dune height on cross-strata architecture: White Sands Dune Field, New Mexico, U.S.A. J. Sediment. Res. 91, 495–506. https://doi.org/10.2110/jsr.2020.138.
Zhou, L., Williams, M.A.J., Peterson, J.A., 1994. Late Quaternary aeolianites, palaeosols and depositional environments on the Nepean Peninsula, Victoria. Australia. Quat. Sci. Rev. 13, 225–239. https://doi.org/10.1016/0277-3791(94)90027-2.